

promoting access to White Rose research papers



Universities of Leeds, Sheffield and York
<http://eprints.whiterose.ac.uk/>

This is an author produced version of an article published in **Proceedings of the IEEE**.

White Rose Research Online URL for this paper:

<http://eprints.whiterose.ac.uk/76237/>

Published article:

Hooper, A, Prata, F and Sigmundsson, F (2012) *Remote sensing of volcanic hazards and their precursors*. Proceedings of the IEEE, 100 (10). 2908 - 2930.

<http://dx.doi.org/10.1109/JPROC.2012.2199269>

Remote Sensing of Volcanic Hazards and their Precursors

Andrew Hooper, *Senior Member IEEE*, Fred Prata and Freysteinn Sigmundsson

Abstract

Ash, tephra and gas ejected during explosive eruptions provides a major far-reaching threat to population, health and air traffic. Lava flows, lahars and floods from ice capped volcanoes can also have a major influence, as well as landslides that have a potential for tsunami generation if they reach into sea or lakes. Remote sensing contributes to the mitigation of these hazards through the use of synthetic aperture radar interferometry (InSAR) and spectroradiometry. In the case of InSAR, displacements of a volcano's surface can be interpreted in terms of magma movement beneath the ground. Thus the technique can be used to identify precursors to eruptions and to track the evolution of eruptions. Recent advances in algorithm development enable relative displacements over many km to be measured with an accuracy of only a few mm. Spectroradiometry on the other hand allows monitoring of a volcanic eruption through the detection of hot-spots, and monitoring and quantification of the ash and SO₂ emitted by volcanoes into the atmosphere. The tracking of ash plumes during eruptions assists in the identification of areas that should be avoided by aircraft. Here we present a review of these two remote sensing techniques, and their application to volcanic hazards.

Index Terms

Volcanoes, Hazards, InSAR, Spectroradiometry.

A. Hooper is with Delft University of Technology, Delft, The Netherlands. e-mail:a.j.hooper@tudelft.nl

F. Prata is with the Department of Atmosphere and Climate, Norwegian Institute for Air Research, Kjeller, Norway. e-mail: fred.prata@nilu.no

F. Sigmundsson is with the Nordic Volcanological Center, Institute of Earth Sciences, University of Iceland, Reykjavik, Iceland. e-mail:fs@hi.is

I. INTRODUCTION

Volcanic hazards include long-distance ash transport, tephra fallout, lava flows, pyroclastic flows, lahars and volcanic gas release, as well as landslides and their potential for generating tsunamis if located close to the sea or a lake. The hazards can have both local and global reach; small eruptions may have devastating effects on their environs, and major explosive eruptions and their eruptive plumes may have global effects on air travel, health and climate. Eruptions often have precursors in the form of volcanic unrest, realized as increased seismicity, elevated ground deformation rates, and increased release of volcanic gas and heat [1]. Such unrest, due to magma movements in the volcanic plumbing system, may culminate either in an eruption or with magma stalling at depth, without reaching the surface.

Various remote sensing techniques can be applied to improve our understanding of volcanic processes, to detect precursory activity to volcanic hazards, and to provide key monitoring data during volcanic hazards. In fact, remote sensing is changing the field of volcanology, to the extent that a new field of “general volcanology” is emerging, resting on various recent technological advances. Remote sensing of volcanic hazards and their precursors via satellites is of central importance in this respect. All imagery of eruptive activity is important to monitor progress of activity, but in this paper we address two types of remote sensing techniques that have advanced in recent decades and are important in the new general volcanology: synthetic aperture radar interferometry (InSAR) for evaluating ground deformation at volcanoes, and spectroradiometry to detect eruption onset, map eruptive products and quantify the amount of ash and gas in eruptive plumes.

Magma movements in the volcano subsurface often lead to detectable signals prior to eruption. Increase in seismic activity is a primary signal of such volcanic unrest, recordable through a network of seismometers on the ground. In some cases, but not all, magma recharging of volcanoes leads to surface deformation of volcanic edifices, often ranging from several to tens of centimeters. This important type of precursor to volcanic activity can be studied by remote sensing, through InSAR. Observations and interpretation of deformation fields on volcanoes can reveal how much, and where, new magma is accumulating in the volcanic plumbing system. InSAR measurements can reveal relative deformation with ~ 10 mm accuracy, providing key information about the nature of volcanic unrest. There have been many successful InSAR

studies, utilizing various radar satellites, of magma accumulation in the volcano subsurface; sometimes such events have preceded eruptions and in other cases no eruption has followed [2] and references therein. The challenge remains to understand when volcanic unrest will lead to an eruption and when it will not. If an eruption occurs, InSAR studies of deformation can reveal co-eruptive deformation, which can be used to constrain the source of the magma, and the magma plumbing systems involved.

Satellite images, in the visible or other frequency bands, record emitted and reflected radiation from the Earth's surface and atmosphere. Data are acquired by radiometers aboard satellites, many of which operate over a wide frequency band. They provide spectroradiometric observations of the precursors to volcanic hazards and once they occur, are able to monitor them in near real-time, sometimes in a continuous manner. Numerous satellites can be used, all of which provide a view on the eruption. Those offering a better compromise between spatial, spectral and temporal resolution are most suitable for contributing to near-real time observations of the progress of eruptive activity. Spectrometry is the topic of the second half of the paper, but we start with an overview of InSAR theory and its application to volcanoes.

II. RADAR INTERFEROMETRY

A. *Synthetic aperture radar imaging*

Synthetic aperture radar (SAR) is a technique that allows high-resolution radar images to be formed from data acquired by side-looking radar instruments, carried by aircraft or spacecraft [3]. A SAR image has both an amplitude and a phase assigned to each resolution element on the ground illuminated by the radar. The amplitude of a SAR image can be interpreted in terms of the scattering properties of the Earth's surface. Because of the ability for radar to work at night and see through clouds, these images can be useful for ascertaining the location and evolution of an eruptive site, at a resolution up to 1–2 m (Fig. 1). Time series of such images can reveal how the geometry and size of eruptive craters change throughout an eruption, and how new landscape is generated. SAR images, if formed in close to real time, can provide critical observations of the progress of an eruption and the conditions at an eruption site during cloud cover and absence of day light; such conditions inhibit the use of radiometers that can otherwise provide spectacular images of eruptive activity. In Iceland, SAR images from both aircraft and satellites have been used extensively to monitor the evolution of eruptive events and the formation of ice cauldrons

during subglacial eruptions. A series of SAR images acquired by an airplane of the Icelandic Coast Guard revealed the evolution of ice cauldrons and eruptive craters during the initial stage of the explosive eruption of Eyjafjallajökull volcano in Iceland in 2010, under fully cloudy conditions [4].

By cross-correlating the amplitude between two SAR amplitude images it is possible to estimate displacements of the ground that occur during the intervening period [5]. The accuracy of this technique is about one tenth of the ground resolution, which for most sensors is 10s of cm. Nevertheless, it can be useful for constraining volcanic events that lead to large deformation, such as the 2005 Afar dike episode [6].

The phase value for each pixel in a single SAR image is not a useful entity on its own, as it contains a pseudo-random phase contribution from the configuration of scatterers within a resolution element on the ground. However, the difference in phase between two images can be interpreted in terms of the change in range from the radar instrument to the ground, as long as the scattering characteristics of the ground remain approximately the same. This forms the basis for InSAR.

B. Two-pass InSAR

Whereas SAR amplitude images can reveal large-scale changes on volcanoes, typically during eruptions or the intrusion of magma to shallow depths, they can rarely reveal the ground deformation in the centimeter range as is typically produced by magma movements deeper within the volcano. Such small movements can be detected by measuring the change in range from ground to satellite using radar interferometry. It is the process of multiplying one SAR image by the complex conjugate of a second SAR image resulting in an “interferogram”, the phase of which is the phase difference between the images [7], [8] and can be measured to within a fraction of the radar wavelength (typically a few mm) for each pixel. An interferogram can be formed between two images acquired at the same time from different positions, or between images acquired at different times from approximately the same position. It is the latter scenario that is of most use in the monitoring of volcanoes, as the resulting interferogram contains the range change due to any deformation of the ground. Such interferograms have in many cases become an essential tool to evaluate pre-eruptive deformation and the status of volcano unrest, as well as co-eruptive deformation taking place during eruptions. Deformation signals prior to

eruptions can reflect various processes, however, and the resulting signals may not be easy to interpret. The clearest deformation signals are produced if magma accumulates at shallow depth prior to eruptions.

Interferograms can only be formed between images acquired by the same sensor, or sensors with near-identical orbits and operating frequencies (Table I). A difference in the position of the satellite between the two acquisitions leads to a geometric contribution to the phase change, which can be approximately corrected for knowing the positions of the satellite and the surface topography. What remains in the interferogram is the displacement of the ground between acquisitions, plus some other nuisance contributions from variations in the propagation properties of the atmosphere, errors in the positions of the satellite and the scatterers on the ground, and changes in the scattering properties of the ground between acquisitions.

What one sees in an interferogram are phase cycles of 2π radians, generally represented by color “fringes” (Fig. 2). If the nuisance terms are sufficiently small, an interferogram reveals a measure of the change in range (distance) from ground to satellite, in the line-of-sight (LOS) direction. This LOS range change can then be interpreted in terms of subsurface magma accumulation and withdrawal, emplacement of magmatic intrusions, and the nature of volcanic processes. SAR satellites operate in approximately polar orbits and can acquire data when travelling from south to north (ascending) and north to south (descending), resulting in look directions that are approximately either to the east or the west (Fig. 2). InSAR is a “two-way system” in the sense that a signal from a radar satellite is scattered back from the Earth and its echo recorded at the satellite. A change in LOS distance of $\lambda/2$, where λ is the wavelength of the SAR system, leads to one full phase cycle change in an interferogram. In other words, each additional $\lambda/2$ of range change results in the identical interferometric phase. The wavelength of SAR systems vary, typically 3.1 cm for X-band, 5.7 cm for C-band and 23.6 cm for L-band systems, with longer wavelengths suffering less from decorrelation noise (see below) but being more impacted by ionospheric interaction, which generally results in long wavelength errors.

It is not possible to interpret interferometric phase directly in terms of absolute range change, as the absolute number of phase cycles is unknown. However, the relative range change between any two points within an interferogram can be estimated by integrating the number of fringes between them. The process of estimating the integrated phase difference between all pixels and a reference pixel is known as phase-unwrapping e.g., [9]. Although most InSAR studies

currently use data acquired from space, it is also possible to acquire data with airborne SARs [10]. Significant advantages are the potential for shorter repeat times in the case of rapidly evolving deformation and the selection of the optimal look direction for the deformation being studied.

The first application of InSAR to the measurement of volcanic deformation was to measure deflation of Mount Etna in 1995 [11]. For other early volcanic applications see reviews by Massonnet and Sigmundsson [12] and Zebker et al. [13]. In the last decade two-pass InSAR has been extensively applied to volcanoes. Studies include observations of inflation and deflation of inferred magma chambers, e.g., [14]–[17], sill and dike intrusion, e.g., [18]–[20], faulting, e.g., [21] and eruption, e.g., [22], [23]. In the early days of InSAR, it was generally only possible to capture an entire eruption in an interferogram, except in the case of long-lived eruptions, like Kilauea. Presently, there are more satellite sensors, and their revisit times are generally shorter, e.g., 11 days for TerraSAR-X and 4 days for the COSMO-SkyMed constellation. Thus eruptions can often now be imaged several times during eruptive activity, especially if images are acquired from more than one viewing geometries (although the cost scales with the number of acquisitions). This can provide a new perspective on complicated process taking place in volcano interiors, as in the case of Eyjafjallajökull volcano in Iceland, when two eruptions occurred in 2010. A small effusive basaltic lava producing eruption occurred on the flank of the volcano from March 20 to April 12, followed by a major explosive eruption from its summit from April 14 to May 22, which disrupted air traffic. TerraSAR-X images were acquired immediately prior to the onset of the flank eruption and every few days after that. Two of the many interferograms that span part of the activity are shown in Fig. 3. Together with Global Positioning System (GPS) geodetic measurements of deformation, the interferograms showed a period of inflation prior to eruption, which could be fit with a series of sills at 4-6 km depth and a dike extending almost to the surface, evolving in the volcano subsurface over three months prior to the eruption [24]. On March 20th the dike breached the surface through a narrow channel feeding the flank eruption. During the entire duration of the flank eruption, there was almost no significant deformation, indicating that the magma feeding the eruption was sourced from great depth; the volume of magma intruded into shallow depths during the preceding months did not deflate. During the subsequent explosive summit eruption, which was preceded by renewed inflation, there was deflation centered on the summit area indicating that some of the erupted

magma was sourced from a pre-existing magma body at some 4–5 km depth. The InSAR study of the 2011 Eyjafjallajökull activity provides an example of how remote sensing can be utilized to study precursors to volcanic activity and constrain magmatic processes taking place in volcano interiors. A fuller elaboration of two-pass InSAR for volcano deformation applications is given in [25], but in many cases the deformation signals are small, and advanced techniques are needed to reliably extract them from InSAR images and interpret them correctly. The main relevant advances in recent years rely on detailed analysis of a time series of SAR images and evaluation of error sources, as explained in the rest of this section. Other recent advances in the field, such as high resolution SAR tomography [26], have added little benefit in terms of monitoring volcanoes, so we do not include them in this review.

C. Time series InSAR

Deformation signals on volcanoes can be subtle (less than 10 mm/yr) and reduction of the noise in interferometric products becomes essential. The primary limitation of InSAR for most sensors is the phase noise due to changes in the scattering properties of the ground. In a SAR image, the amplitude and phase for each pixel comes from the coherent sum of contributions from all scatterers within the associated ground resolution element (Fig. 4a). Relative movement of these scatterers, or a change in the look direction, causes the scatterer contributions to sum differently, an effect known as decorrelation [27]. The degree of relative movement of the scatterers depends on their size, as larger scatterers tend to be more stable. As more energy is returned from scatterers of about the same size as the wavelength of the radar system, longer wavelength systems, such as L-band, display the least decorrelation. If the decorrelation term is a significant fraction of a phase cycle, the integration of phase difference between points becomes unreliable. Scattering characteristics of the ground may also change completely because of snow cover; one SAR image in snow-free conditions and another with significant snow on the ground can not be used to form an interferogram. This severely limits the use of InSAR for volcano studies at high latitudes, and high on volcanic edifices worldwide that have variable ice and snow cover.

The effect of decorrelation can be mitigated somewhat in two ways, each at the cost of resolution. Firstly, by bandpass filtering each image prior to interferogram formation [28]. A change in look direction can be interpreted in terms of a frequency shift, and filtering ensures that only the overlapping frequencies are retained. Secondly, by filtering after interferogram formation

[29]. This can also be achieved by summing the interferometric values of many neighboring resolution elements, which is known as “multilooking”. As long as the signal does not vary significantly across the area in the multilooked element, the signal in each element reinforces, whereas the decorrelation noise does not. In the case of extreme decorrelation however, such as when the scatterers are inherently non-stationary objects such as leaves on trees, these filtering techniques fail to mitigate decorrelation sufficiently.

The second limitation of InSAR, particularly in the case of small deformation and strain, is that other non-deformation contributions to the InSAR phase can mask the deformation signal. After correction for topography, the interferometric phase consists of the following contributions:

$$\phi = W\{\phi_{def} + \phi_{atm} + \Delta\phi_{orb} + \Delta\phi_{\theta} + \phi_N\}, \quad (1)$$

where ϕ_{def} is the phase change due to movement of the pixel in the satellite line-of-sight direction, ϕ_{atm} is the difference in atmospheric phase delay between passes, $\Delta\phi_{orb}$ is the residual phase due to orbit errors, $\Delta\phi_{\theta}$ is the residual phase due to look angle error (commonly referred to as DEM error, although there is also a contribution from the subpixel position of the phase center of the resolution element), ϕ_N is the interferometric phase noise, typically dominated by the decorrelation effect referred to above, and $W\{\cdot\}$ is the wrapping operator that drops whole phase cycles, because phase can only be measured in terms of the fractional part of a cycle. The atmospheric term in particular correlates partly with topography and can therefore be very significant on volcanoes with high relief. As deformation due to changes in pressure of magma sources is commonly also centered on the highest part of a volcano, disentangling the two may not be trivial.

One approach for reducing these nuisance terms is the summing or “stacking” the unwrapped phase of many conventionally formed interferograms [30]. The deformation signal reinforces, whereas other signals typically do not. However this approach is only appropriate when the deformation is episodic or purely steady-state, with no seasonal deformation. Even then it is not optimal, as the non-deformation signals are reduced only by averaging rather than by explicit estimation. Algorithms for time series analysis of SAR data have been developed to better address the two aforementioned limitations of conventional InSAR. The first limitation is tackled by using phase behavior in time to select pixels where decorrelation noise is minimized. The second limitation is addressed by estimating the non-deformation signal by a combination of modeling

and filtering of the time series. The time series algorithms fall into two broad categories, the first being persistent scatterer InSAR, which targets pixels with consistent scattering properties in time and viewing geometry, and the second being the more general small baseline approach.

1) *Persistent scatterer InSAR*: Decorrelation is caused by contributions from all scatterers within a resolution element summing differently. This can be due to relative movement of the scatterers, a change in the looking direction of the radar platform, or the appearance/disappearance of scatterers, as in the case of snow cover. If however one scatterer returns significantly more energy than other scatterers within a resolution element, the decorrelation phase is much reduced (Fig. 4). This is the principle behind a “persistent scatterer” (PS) pixel, also referred to as a “permanent scatterer”. In urban environments, the dominant scatterers are commonly roofs oriented such that they reflect energy directly backwards, like a mirror, or the result of a “double-bounce”, where energy is reflected once from the ground, and once from a perpendicular structure, causing it to return in the direction from whence it came [31]. Dominant scatterers can also occur in areas without manmade structures, e.g., appropriately oriented rocks or the largest and highest-rising blocks in lava fields, but there are fewer of them, and they tend to be less dominant. No filtering or multilooking is applied in PS processing as these techniques degrade resolution, thereby adding more scatterers to each resolution element. As non-dominant scatterers are considered as noise sources for PS pixels, increasing their number can lead to an increase in decorrelation noise.

PS algorithms operate on a time series of interferograms all formed with respect to a single “master” SAR image. The first step in the processing is the identification and selection of the usable PS pixels. There are two approaches to this; the first relies on modelling the deformation in time, e.g., [32], [33] and the second relies on the spatial correlation of the deformation, e.g., [34], [35]. In the first approach, the phase is unwrapped during the selection process, by fitting a temporal model of evolution to the wrapped phase difference between pairs of nearby PS, although later enhancements to the technique allow for improvements to the unwrapping that are not model-based, to allow monitoring of persistent scatterers undergoing highly non-linear deformation in time. In the second approach a phase-unwrapping algorithm is applied to the selected pixels without assuming a particular model for the temporal evolution [36]. In both approaches, deformation phase is then separated from atmospheric phase and noise by filtering in time and space; the assumption is that deformation is correlated in time, atmosphere is correlated

in space but not in time, and noise is uncorrelated in space and time. In comparative studies between the two approaches, estimates for the deformation estimates tend to agree quite well, but the second approach tends to result in better coverage, particularly in rural areas [37], [38].

The result of PS processing is a time series of displacement for each PS pixel, with noise terms much reduced. This enables detection of subtle processes as demonstrated on Mount Etna in Fig. 5. During this non-eruptive period, deformation is visible related to gravitational spreading, magma recharge and the cooling of lava.

The persistent scatterer InSAR technique has the advantage of being able to associate the deformation with a specific scatterer, rather than a resolution element of dimensions dictated by the radar system, typically on the order of several metres. This allows for very high resolution monitoring of infrastructure. From the point of view of volcano deformation studies, however, this level of detail is generally not required, although it can be useful in separating crustal deformation from the local deformation of specific structures.

2) *Small baseline InSAR*: A drawback of the PS technique for volcanic applications is that the number of PS pixels in a volcanic environment may be limited. For non-PS pixels, containing no dominant scatterer, phase variation due to decorrelation may be large enough to obscure the underlying signal. However, by forming interferograms only between images separated by a short time interval and with a small difference in look direction, decorrelation is minimized, and for some resolution elements can be small enough that the underlying signal is still detectable. Decorrelation is further reduced by bandpass filtering as mentioned above [28]. Pixels for which the filtered phase decorrelates little over short time intervals are the targets of small baseline methods.

Interferograms are formed between SAR images that are likely to result in low decorrelation noise, in other words, those that minimise the difference in time and look direction. Obviously it is not possible to minimise both of these at once, so assumptions have to be made about the relative importance, based on the scattering characteristics of the area of interest. In many small baseline algorithms, the interferograms are then multilooked to further decrease decorrelation noise [39]–[41]. However, there may be isolated single ground resolution elements with low decorrelation noise, such as a small clearing in a forest, that are surrounded by elements with high decorrelation noise, for which multilooking will increase the noise. Therefore, other algorithms have been developed that operate at full resolution [42], [43], with the option to reduce resolution

later in the processing chain by “smart” multilooking. Pixels are selected based on their estimated spatial coherence in each of the interferograms, using either standard coherence estimation [44] or enhanced techniques, in the case of full-resolution algorithms. The phase is then unwrapped either spatially in two dimensions [9], or using the additional dimension of time in 3-D approaches [36], [41], [45]. In the case of [41], the unwrapping algorithm relies on a model of deformation in time, similar to the persistent scatter algorithm of [32]. At this point the phase can be inverted to give the phase at each acquisition time with respect to a single image, using least-squares [40], singular value decomposition [39], or minimization of the L^1 -norm [46]. Separation of deformation and atmospheric signals can be achieved by filtering the resulting time series in time and space, as in the PS approach. Alternatively, if an appropriate model for the evolution of deformation in time is known, the different components can be directly estimated from the small baseline interferograms [47].

Although different pixels may be utilised in the small baseline analysis than the PS analysis, the results are typically similar. An example application to Campi Flegrei, Italy is shown in Fig. 6. The mean displacement map shows the spatial variation of the uplift and the time series for a specific point shows that the uplift accelerated between 2004 and 2006, in agreement with leveling measurements. Campi Flegrei is an area of persistent volcanic unrest in the highly populated Pozzuoli Bay area of Naples, with millions of people exposed to potential volcanic hazards in the area; understanding the subsurface magmatic systems is therefore of high value.

3) *Combined time series InSAR*: Because persistent scatterer and small baseline approaches are optimized for resolution elements with different scattering characteristics, they are complimentary, and techniques that combine both approaches are able to extract the signal with greater coverage than either method alone [43], [48]. An application to Eyjafjallajökull volcano is shown in Fig. 7 where two sill intrusion episodes are captured during the period from 1993 to 2000 [49]. This gives an example of how InSAR deformation studies can be used to study long term volcanic unrest; in the case of Eyjafjallajökull volcano unrest occurred over an 18 year interval, from 1992 until the eruptions in 2010. Another application to Hekla volcano (Fig. 8) demonstrates the potential to monitor the full deformation cycle of a volcano that is continuously receiving magma inflow and has intermittent eruptions [50].

D. Tropospheric correction

Applying InSAR to volcanoes with high topographic relief, such as most stratovolcanoes, is particularly challenging due to a correlation of atmospheric phase delay with topography. Delay of a radar signal as it propagates through the atmosphere is principally due to interaction with the ionosphere and the lower troposphere but it is the tropospheric delay that leads to the correlation; the higher the ground is, the shorter the fraction of the troposphere that is traversed by the signal, and the smaller the phase delay. Variation in the phase delay from this effect can be 10s of cm, even when considering only the difference between the delay of two acquisitions that is present in an interferogram [51]. Time series algorithms rely on estimating the differential atmospheric delay by filtering in time and space. However, separating non-steady deformation from atmospheric delay is challenging, and even in the case of a steady deformation rate, significant improvements in deformation accuracy can be achieved by reducing the atmospheric phase delay before filtering. In some cases this can be achieved by estimating the correlation between unwrapped interferometric phase and topography, in a non-deforming area [52]. However, this is only possible if the density of coherent pixels is such that the phase can be reliably unwrapped from low altitudes to high altitudes. Stratovolcanoes, in particular, commonly have highly vegetated slopes that can lead to an absence of coherent pixels between the base and summit. Hence, several phase cycles can be missed in the phase-unwrapping process. In this case the tropospheric phase delay may be estimated from external data in order to correct the interferometric phase before unwrapping. The external data can come from weather models [53], continuous GPS stations [54], or spectrometer measurements, optionally combined with weather models or GPS [55], [56]. An example of phase correction using external data is shown in Fig. 9 for Colima Volcano. From a global atmospheric weather model and spectrometer measurements, Pinel et al. [57] estimated that there could be up to six missing interferometric fringes between coherent pixels at the base of the volcano and the summit. After correction for the atmospheric phase in each interferogram, the remaining phase was analyzed using a combined time series analysis technique [43]. The results show that there was no significant large-scale deformation between 2003 and 2006.

III. SPECTRORADIOMETRY

A. *Historical background*

Since the late 1960's Earth orbiting satellites have made routine measurements of the emitted and reflected radiation from the Earth's surface and atmosphere. The instruments used were designed to study and understand the atmosphere, to improve weather forecasting models and to monitor cloud systems, storms, severe weather and later to measure the temperature of the oceans. By the 1970's, with the introduction of the Landsat program, applications were extended to studies of changes in the land surface. The first types of instruments used were scanning radiometers, sensitive in the wavelength range 0.5–15 μm , from the visible through to the infrared and could assess the brightness of the surface and atmosphere, also called the albedo, as well its temperature and moisture vertical structure. As technology advanced, broadband scanning radiometers were replaced by multichannel narrowband sensors able to image the Earth using whisk broom, push broom and staring configurations. Spectral and spatial resolutions were improved to the extent that a new range of applications became practical, including applications in natural hazards, such as flooding, landslides, fire monitoring, and volcanic activity. Table II provides an overview of the main advances in satellite technology used to monitor the Earth, and lists the main instruments used in natural hazards applications.

A notable feature of the advance of space-borne technology is the increase in the spatial resolution of the imagery, from about 100 m pixels in the 1970's to less than 1 m by 2001. This dramatic increase has led to an increase in the number and type of applications that the data may be used for; for example, with the advent of 1 m spatial resolution imagery applications in town planning, farm-scale management, hydrology, geology and natural disaster monitoring (e.g. wildfires) have become almost routine. It is important to make a distinction between the sensors with very high spatial resolution, commonly commercially oriented, and the programmatic, operational and research oriented sensors used mostly for Earth observation. These sensors are typified by the flagship NASA Earth observation sensor the Moderate resolution Imaging Spectroradiometer–MODIS. Earlier Earth Observing (EO) sensors such as the Advanced Very High Resolution Radiometer (AVHRR) consisted of just four or five bands in the visible to thermal infrared, compared to the 36 bands of MODIS aboard the Terra and Aqua satellites. The advantages of higher spectral resolution are apparent considering the breadth and scope of

applications that have been developed. Table III lists the main characteristics of MODIS, which can be considered as typical of spectroradiometers used by many international space agencies including, ESA, Eumetsat, and NASDA.

From a thematic point of view it has been found that spatial resolutions in the reflective channels of 250 m meet many of the requirements needed for global Earth observation including natural hazard monitoring, whereas a lower resolution of 1–4 km is adequate in the emissive or thermal channels. Thus MODIS and its predecessors, such as AVHRR have utilised spatial resolutions that are not wholly compatible with applications in volcanology. There is a compromise between swath width, repetition rate and spatial resolution whereby it is not feasible to obtain high spatial resolution (~ 1 m) and daily coverage from a single satellite platform. The design and development of sensors like MODIS, which has a resolution of 250 m to 1 km, require many compromises and it should be noted that none of the current operational sensors have been specifically designed for natural hazard monitoring, let alone for studies of volcanic unrest. Nevertheless, the general utility and availability of imagery from operational and commercial satellite systems (we do not deal with military and defence related sensors) has generated a large and varied list of uses in natural hazards, of which we concentrate on those applicable to volcanic activity. Of particular interest for monitoring volcanic unrest is the geostationary SEVIRI (Spin-Enhanced Visible and Infrared Imager) instrument on board the MSG (Meteosat Second Generation) satellite platform, as this can be used to detect "hot-spots", track volcanic clouds and provide quantitative estimates of ash and SO_2 . These aspects are discussed in more detail in later sections

B. Spectroradiometry principles

Spectroradiometric measurements from Earth observation platforms have been made from the ultra-violet (wavelengths down to $0.3 \mu\text{m}$) to beyond the thermal infrared (wavelengths up to $15 \mu\text{m}$). It is sometimes useful to divide the electromagnetic spectrum (EM) into parts in order to illustrate important applications and also to understand the basic principles of the physics of the interaction of EM energy with the atmosphere and surface. It is not the intention of this paper to provide an authoritative discussion of the physical principles of spectroradiometry as these may be found in the many good books on the subject (e.g. [58], [59], however some basic comments follow. The radiation received by a satellite sensor arrives there after undergoing a

series of interactions with the Earth's surface and atmosphere, including absorption, scattering (multiple) and emission. Assuming that we may consider at least the reflective part of the EM spectrum, that is the interactions involving sunlight as the source of radiation, as separate from the emissive part, then the radiance received at a single monochromatic wavelength, λ may be written,

$$I_{\lambda,s} = \frac{I_{\lambda,o}}{\pi} \mathcal{R}_\lambda \exp\{-\tau(\lambda)/\mu\} + I_{\lambda,a}, \quad (2)$$

where $I_{\lambda,s}$ is the spectral, directional radiance measured by the sensor, $I_{\lambda,o}$ is the total solar irradiance incident at the surface, $I_{\lambda,a}$ is the radiance contribution from the atmosphere, μ is the cosine of the zenith view angle, τ is the extinction optical depth of the atmosphere (due to gases, molecules and aerosols), and \mathcal{R}_λ is the bidirectional surface reflectance function. It is understood that all of the radiance quantities are direction dependent and that in reality the radiances are not monochromatic but represent the radiance integrated over a band of wavelengths convolved with the instruments' response function. The solar irradiance is composed of direct and diffuse parts, and when incident on a flat surface may be written,

$$I_{\lambda,o} = S_o \exp\{-\tau(\lambda)/\mu_i\} + \int_o^{\pi/2} \int_{-1}^1 I_{\lambda,d}(\mu', \phi') P(\mu, \phi; \mu', \phi') d\mu' d\phi' \quad (3)$$

where P is the phase function governing the way that a scatterer (e.g a particle or aerosol) distributes energy in three dimensional space, μ_i is the cosine of the solar zenith angle, and μ' and ϕ' are the cosine of the zenith view angle and azimuth viewing angle, respectively. $I_{\lambda,d}$ is the diffuse component of the downwelling atmospheric radiance, and S_o is the top of the atmosphere solar irradiance. A typical land surface application for a space-based spectroradiometer is to determine the reflectance of the surface from a measurement $I_{\lambda,s}$ and then infer some other properties of the surface, for example the state of the vegetation. One measurement severely underconstrains the problem and it is now recognised that accurate surface property retrievals are only possible using many channels (e.g. a hyperspectral instrument). It is commonly the case that rather than retrieve some property of the surface, we are also interested in the composition of the atmosphere and wish to retrieve, for example, the aerosol content. In this case it is necessary to solve for the source term ([60]),

$$J(\tau; \mu, \phi) = \frac{\varpi}{4\pi} \int_0^{2\pi} \int_{-1}^1 I(\tau; \mu', \phi') P(\mu, \phi; \mu', \phi') d\mu' d\phi' + \frac{\varpi}{4\pi} S_o P(\mu, \phi; -\mu_0, \phi_0) e^{-\tau/\mu_0}. \quad (4)$$

ϖ is the single-scattering albedo (the ratio of the cross sections due to scattering and extinction). When the goal is to determine the gaseous content, then after neglecting scattering effects the governing radiative transfer may be written,

$$I_{\lambda,s} = I_{\lambda,o} \exp\{-\rho k_{\lambda} L\}, \quad (5)$$

where ρ is the gas concentration, L is the path length and k_{λ} is the absorption cross-section. This is the Beer-Bouguer-Lambert law. In practice it is often necessary to include the effects of the surface (the Bi-directional Reflectance Distribution Function or BRDF), scattering effects (the phase function) in order to accurately retrieve gaseous amounts. An example of how the retrieval is done for volcanogenic SO_2 using ultra-violet measurements from the Ozone Monitoring Instrument (OMI) may be found in [61].

In the thermal (emissive) parts of the EM spectrum with scattering negligible, the radiative transfer equation (RTE) used in remote sensing applications takes the form (e.g. [62]),

$$I_{\lambda,s} = \tau_{\lambda,0} B_{\lambda}[T_s] + \int_{p_s}^0 B_{\lambda}[T(p)] \frac{\partial \tau_{\lambda}}{\partial p} dp, \quad (6)$$

where p pressure, T is temperature, T_s is surface temperature, τ_{λ} is wavelength dependent atmospheric transmittance, τ_0 is the total transmittance of the atmosphere from the top of the atmosphere to the surface, and B is the Planck function. For simplicity we have assumed a black surface, but it is straightforward to include a non-unity spectral emissivity. The information to be retrieved from a set of measurements $I(\lambda, s)$ is contained in τ_{λ} , which varies according to the amount and type of gas along the atmospheric path. A great deal of mathematical technique has been developed to solve the RTE and retrieve temperature and composition profiles (e.g. [63]).

As a simple example of the application of (5) for remote sensing of volcanic ash (see later), consider two monochromatic infrared measurements I_1 and I_2 of a uniform ash cloud at temperature T_c overlying a black surface (e.g. the sea) with temperature, T_s . The RTE for each of these measurements may be written ([64]),

$$I_1 = \epsilon_1 B_1[T_c] + (1 - \epsilon_1) B_1[T_s], \quad (7)$$

and

$$I_2 = \epsilon_2 B_2[T_c] + (1 - \epsilon_2) B_2[T_s], \quad (8)$$

where ϵ_1 and ϵ_2 are infrared emissivities of the ash cloud at the corresponding wavelengths. To obtain these equations from (5), the atmospheric term (2nd term of the right-hans side of (5)), has

been approximated by an isothermal cloud of temperature T_c and the atmosphere below the cloud is assumed to be transparent. These simultaneous equations can be linearised to temperatures and solved to determine the ratio of the emissivities at the two wavelengths, which in turn is related to the ratio of the absorption coefficients. This ratio is an excellent discriminant for silicate particles, taking a value quite different to that for an atmosphere containing only water vapour, water droplets and ice clouds.

The region of the EM spectrum most commonly used to observe the Earth and its atmosphere is illustrated in Fig. 10. There are three panels in this figure, each showing a different portion of the EM spectrum. The solid black line in each panel is the vertical transmission of radiation through the atmosphere, looking downwards through the atmosphere towards the Earth's surface, for a standard atmosphere. When the transmission is unity the atmosphere is completely transparent to radiation at that wavelength; when the transmission is zero, then no radiation from the surface reaches the top of the atmosphere and the region is opaque at that wavelength. In Fig. 10(a), below about $0.3 \mu\text{m}$ transmission is zero or close to it, and remote sensing of the surface from space is not possible. This region is commonly referred to as the "solar blind" because all of the insolation is absorbed by atmospheric gases, principally ozone (O_3), high in the atmosphere—there is no incoming solar energy reaching the surface. Just above this region, from $0.3 \mu\text{m}$ onwards, ultra-violet radiation is absorbed and scattered preferentially by O_3 and SO_2 and this region is used to measure these gas concentrations. The Ozone Monitoring Instrument (OMI) is a good example of a satellite instrument exploiting this part of the EM spectrum, and it has been used very successfully to look at passive degassing SO_2 volcanic emissions as well as explosive SO_2 emissions reaching high into the atmosphere. Beyond the UV region and into the visible part of the spectrum, there are many wavelength regions that are transparent and can be used to remotely sense the Earth's surface. Satellite spectroradiometers like MODIS, Advanced Spaceborne Thermal Emission and Reflection Radiometer (ASTER) and the very high spatial resolution cameras on IKONOS, SPOT and the Pleiades constellation are used to monitor changes on the Earth's surface and have many applications in volcanology such as: geological mapping, change detection, hot-spot identification and for studying lava flows, e.g., [65].

Beyond the visible and near-infrared part of the EM spectrum between $1\text{-}5 \mu\text{m}$, sometimes referred to as the mid-infrared, there is an interplay between scattered sunlight and emitted thermal radiation, with contributions from both to radiation reaching a satellite sensor (middle-

panel 10(b)). At approximately $3 \mu\text{m}$ the contributions are almost equal. This is an interesting portion of the spectrum for geological applications because many exposed minerals have spectral features between $1\text{--}2.5 \mu\text{m}$. As a result there are several spaceborne and airborne sensors designed to operate in these reflective regions, including the Advanced Land Imager (ALI) and Hyperion both operating with hundreds of channels between $0.9\text{--}1.6 \mu\text{m}$. The applications in this region are mostly for mapping and geological identification of economically important minerals in exposed settings.

Another important application in this spectral region for volcanology lies in the use of bands centred between $3\text{--}4 \mu\text{m}$ for “hot-spot” identification, e.g., [66]. The Planck function has a peak in radiance in this wavelength region when the source is of high temperature $\sim 1000 \text{ K}$. Fig. 11 shows Planck radiance curves as a function of wavelength for temperatures typical of warm terrestrial temperatures and for a hot source. It can be seen that as temperature increases the peak in radiance shifts towards lower wavelengths. For typical land surface temperatures ($\sim 300 \text{ K}$) the peak is just beyond $11 \mu\text{m}$, whereas for a hot fire or lava flow ($\sim 1000 \text{ K}$) the peak is closer to $4 \mu\text{m}$. As temperatures increase further the peak moves to lower wavelengths. The radiation received at the satellite sensor consists of both reflected and emitted components and because the pixel size is finite and commonly much larger than the area of the hot lava, any retrieval of the temperature of the hot lava must account for these effects. Multiple bands have been also been used to constrain the retrieval [67], but changing wavelength also changes reflected sunlight and unless corrections are applied, the temperature and area of the lava will be in error. The problem of reflected sunlight disappears when observing at night. The “MODVOLC” near realtime thermal hot spot alert system (<http://modis.higp.hawaii.edu> [68]) is a good example of the exploitation of the mid-infrared EM spectrum for volcanological applications.

Figure 10c shows the portion of the EM spectrum from about $5 \mu\text{m}$ to $20 \mu\text{m}$. This region is rich in gas absorption features and has been used by atmospheric physicist to make vertical retrievals of gas composition and also retrieve the vertical temperature profile. The main gases contributing to absorptions across this region are shown in the upper part of the panel. Each gas absorbs in very specific wavelength regions and the spectral variation of absorption across each band can be used to determine the amount and vertical structure of the gas. Between $8\text{--}13 \mu\text{m}$ lies a region with less absorption, the so-called “dirty” atmospheric window, where it is possible to sense the Earth’s surface and determine, quite accurately ($\pm 0.5 \text{ K}$) the temperature of the

sea surface. It is also possible to determine land surface temperatures but with less accuracy ($\pm 1\text{--}2$ K), mostly due to variations in land surface emissivity. There are also two important features in this window region that have been used to study volcanic phenomena. These are the SO_2 absorption feature near to $8.6 \mu\text{m}$ and the peculiar spectral absorption of silicate particles between $8\text{--}12 \mu\text{m}$. These are discussed in more detail later.

There are several operational and research satellite sensors that exploit this thermal infrared region of the EM spectrum, and some of these are indicated on the figure. Over the last few years there has been a move towards utilising high-spectral resolution infrared spectrometers and interferometers to probe the atmosphere and retrieve a variety of gases. Good examples of these sensors are the Infrared Atmospheric Sounder Interferometer (IASI) and the Atmospheric Infrared Sounder (AIRS), each with 1000's of channels and ability to provide vertical information on the temperature, moisture and gas composition of the atmosphere. The inset images in panel (c) show examples of SO_2 retrieval using the AIRS sensor, and a volcanic ash retrieval (see later) using the SEVIRI (Spin-Enhanced Visible and Infrared Imager) sensor. Whereas these sensors utilise channels within important CO_2 bands, so far it has not been possible to retrieve volcanogenic CO_2 with any degree of certainty, although there are on-going efforts using the Japanese GOSAT (Greenhouse gases Observing Satellite; http://www.gosat.nies.go.jp/index_e.html) instrument and plans to use the second Orbiting Carbon Observer (OCO-2; http://www.gosat.nies.go.jp/index_e.html), both systems oriented towards observing CO_2 .

C. Mapping applications in volcanology

There are four main areas of volcanology where use of reflected and emitted radiation measurements from remote sensing satellite sensors have made a major impact: (1) mapping of flows and deposits., e.g., [69], (2) monitoring of volcanic eruption through detection of hot-spots, e.g., [70], (3) heat flux measurements to monitor effusive eruptions and (4) monitoring and quantifying the ash and SO_2 emitted by volcanoes into the atmosphere. Ramsey and Flynn [71] describe the use of NASA's Earth Observing system for making applications in volcanology. An example of the first application is given in Fig. 12, which shows the lava flow and ash clouds emitted by the June, 2011 Nabro (13.4°N , 41.7°E) eruption in Eritrea. This daytime image was acquired on July 6, 2011 by the ASTER instrument on NASA's Terra spacecraft, with spatial resolution of 30 m. Hot lava flows and lava in the summit crater are displayed in shades of red and white using data

from the thermal infrared bands. The dark-grey clouds are ash-laden and extend some distance from the eruption site towards the south. It is very clear from these high-spatial resolution data that there was ash in the eruption and the lava flow is clearly delineated, but Nabro also produced copious amounts of SO_2 ($> 1 \text{ Tg}$). The SO_2 clouds were observed by several earth observing satellites (e.g. OMI, SEVIRI and AIRS) and these high-temporal resolution data with sufficient but lower spatial resolution, tracked the SO_2 clouds for many days as it spread northwards and then eastwards at altitudes of at least 10 km. However, very little ash was transported away from the volcano.

A second example demonstrating the capability of combining Landsat and ASTER imagery to map volcanic landscapes is shown in Fig. 13. This image is a combination of Shuttle radar imagery (Shuttle radar topography mission–SRTM), Landsat thematic mapper data and ASTER thermal imagery and was made by NASA’s Jet Propulsion Laboratory. The data have been combined and manipulated to show surface elevation and map the lava flows from Nyiragongo volcano in the Congo. The eruption occurred on January 17, 2002, and the lava flows reached the city of Goma on the north shore of Lake Kivu. Approximately 350,000 people fled from the advancing lava, many of them into neighboring Rwanda. Estimates of fatalities range from 60–100 people, with as many as 500 people reported injured with burns, fractures and gas intoxication. The partial map of the recent lava flows (red overlay on Fig. 13), was made using NASA TIR ASTER imagery at 90 m resolution including a complete mapping of the flows into Goma as of January 28, 2002. Lava is also apparent within the volcanic crater and at a few other locations. Goma has a light pink speckled appearance along the shore of Lake Kivu; the image appearance relying on the use of Landsat bands 3, 2 and 1 at 30 m resolution, assigned to the red, green and blue display channels, respectively. Finally, the SRTM data also at 30 m resolution have been used to provide the elevation information.

D. Hot-spot detection and heat flux

The importance of being able to detect thermal anomalies from satellites has been highlighted in a number of papers, e.g., [72], [73], [67], [70] and operational tools now exist to provide early warnings of possible volcanic activity, e.g., MODVOLC [74], the Robust Satellite Technique [75] and a hybrid approach [76]. The principle of the detection is based, in its most fundamental level, on instances of high radiance detected at $\sim 3.7 \mu\text{m}$ compared with surrounding pixels and

against “normal” or climatological radiance behaviour. Often an alert is only issued if there is a sequence of anomalously high radiances from the same or adjacent pixels. These thermal alerts have proved to be extremely helpful for detecting change at restless volcanoes. There are some instances where care must be take. For example, hot spots can also arise from the lighting of fires and these can happen on the slopes of active volcanoes. Accurate geolocation and high spatial resolution sensors are therefore required to reduce ambiguity and increase confidence in these alerts. For global applications MODIS, AVHRR and ATSR (Along-Track Scanning Radiometer) have proved to be very useful, whereas for detailed studies, ASTER data are generally preferred because of the higher spatial resolution. A summary of the use of an EO sensor for detecting volcanic hot spots can be found in [67].

Related to the detection of hot-spots, the emissive channels of several satellite sensors may be used to quantify the heat flux from effusive style eruptions and lava flows. Basaltic lava flows are relatively easy to detect in high spatial resolution infrared data, whereas pyroclastic flow activity is less easy, partly because of spatial resolution issues, leading to mixed pixel effects, but also because the source may be cooler (~ 500 K), and there may be more particles, gases and aerosols interfering with the signal reaching the satellite. In an ideal case of a uniform high temperature source, the heat flux can be determined using the Planck function,

$$B_{\lambda} = \frac{\epsilon c_1}{\pi \lambda^5 [\exp(c_2/\lambda T) - 1]}, \quad (9)$$

where B_{λ} is the spectral radiance in $\text{W m}^{-2} \mu\text{m}^{-1} \text{sr}^{-1}$, c_1 and c_2 are the constants with values $3.742 \times 10^{-16} \text{ W m}^2$, $1.44 \times 10^{-2} \text{ m K}$, T is temperature (K), λ is wavelength (μm) and ϵ is the emissivity (dimensionless) of the radiating surface. Because this is applied to hot, dark surfaces the effect of reflected sky radiation can be neglected. Planck’s equation can be inverted to determine the temperature, commonly referred to as the brightness temperature as it is a wavelength dependent quantity and not the actual thermodynamic or kinetic temperature of the material. Under ideal conditions the radiating temperature is close to the actual kinetic temperature of the hot surface and assuming that only a fraction f of the pixel is affected by the hot source, the radiant heat (W per pixel) may be written [77]:

$$Q = \sigma \epsilon A [f T^4 + (1 - f) T_b^4], \quad (10)$$

where σ is Stefan-Boltzmann’s constant ($5.67 \times 10^{-8} \text{ W m}^{-2} \text{ K}^{-4}$), A is the surface area, and T_b is a background temperature representing, for example, the cooler crust of a lava flow. The

goal is to estimate Q accurately and therefore it is also necessary to estimate f and T_b . Several schemes to estimate Q have been suggested, using various models together with multi-spectral satellite measurements (e.g., [72], [73], [78], [79]).

E. Remote sensing of volcanic ash

The recent eruptions of Eyjafjallajökull, Iceland (April–May, 2010), Grímsvötn, Iceland (May, 2011), Puyehue-Córdon Caulle, Chile (June–July, 2011) and Nabro, Eritrea (June, 2011) brought international attention to the hazard posed by volcanic ash to commercial jet aircraft and caused airspace closures and financial losses to the aviation industry and beyond. The main hazard to jet aircraft is caused from the melting and fusing of silicate-rich material (volcanic ash) to engine turbo blades, vanes and other hot parts of the combustion engine. If airflow is restricted, the jet engine “flames-out” and stalls [80]. This has happened on a few occasions, most notably after the eruption of Galunggung, Java in June 1982 and after the eruption of Redoubt, Alaska in December 1989. Many incidents were also recorded following the eruption of Pinatubo, Philippines in June 1991. These incidents and other less serious encounters have catalyzed the use of Earth observing satellites for identifying and quantifying volcanic ash dispersal in the atmosphere. Early work on the problem by Prata [81] demonstrated that two channels in the infrared between 10–12 μm could be used to discriminate ash from hydrometeors (water droplets and ice), provided the atmosphere was not too humid. Because the spectral variation of the infrared refractive index of silicates is different (so-called ‘reverse’ absorption) to that of water and ice, the spectral variation of absorption of infrared radiation is also different. Thus the ratio of the absorption coefficients at the two wavelengths provides a means to discriminate ash clouds from other meteorological clouds (see earlier for the RTE explanation). An easy way to visualise this effect is to subtract the temperatures between two satellite measurements at $\sim 11 \mu\text{m}$ (MODIS channel 31, see Table III) and $\sim 12 \mu\text{m}$ (MODIS channel 32). Negative differences are caused by absorption due to silicate particles (volcanic ash), whereas positive differences are due to water vapour, water droplet and ice cloud absorption effects.

Ash from the recent (5 June, 2011) eruption of Puyehue-Córdon Caulle travelled around the Southern Hemisphere three times and caused aviation problems in South America, South Africa, Australia and New Zealand. Fig. 14 shows a MODIS true-color image of the rising column of ash from Puyehue-Córdon Caulle at the start of the eruption on 5 June, 2011. As the ash

clouds rose and reached the upper troposphere, the strong westerly winds there caused rapid transport and dispersion. Detecting these hazardous clouds from space became a priority for global aviation on three continents.

To illustrate ash detection, Fig. 15 shows a montage of volcanic ash detected using the ‘reverse’ absorption technique for the eruption of Puyehue-Córdon Caulle, in southern Chile. In this case data from the AIRS sensor have been used. AIRS is an etalon spectrometer [82] that provides global imagery every two days in more than 2000 channels. These extra channels improve the detectability of trace amounts of ash in the atmosphere.

Detecting ash using satellite sensors has been a great success and so far no aircraft have been lost due to ash encounters. As the eruption of Eyjafjallajökull illustrated, avoidance may be necessary, but large financial losses, passenger disruption and transport chaos occurred as a result of preventing aircraft from flying. Regulators therefore quickly decided to impose ash concentration limits which could be used to assess the ash hazard and allow, or prevent, aircraft from using airspace in an orderly fashion (prior to April 2010 there were no agreed ash concentration limits and there are still no quantitative limits outside European airspace). The new limits were organised into three levels that could be used to specify zones: below 0.2 mg m^{-3} , in which flying is permitted, up to 2 mg m^{-3} a zone with enhanced procedures, and a ‘no fly’ zone for concentrations greater than 4 mg m^{-3} . These zones apply in European airspace and have not been accepted for global use. The imposition of zones based on ash concentrations implies that concentrations can be measured and forecast. Prata and Grant [64] and Prata and Prata [83] have shown that ash mass loadings can be determined from thermal infrared satellite data with a lower detection limit of about 0.2 g m^{-2} and a standard error of $\pm 0.15 \text{ g m}^{-2}$ and hence can meet the goal of determining concentration zones. To forecast concentrations however, requires accurate dispersion models and most importantly, knowledge of the eruptive behavior of the volcano, commonly referred to as the eruption “source” term [84]. Stohl *et al.* [85] have shown that by constraining dispersion model simulations with satellite retrievals it is possible to determine important aspects of the source term, for example the mass emission rate, the vertical structure of the emissions and the particle size distribution. Fig. 16 shows an example of volcanic ash mass loading retrievals for the Eyjafjallajökull eruption on May 17, 2010 when airspace over the United Kingdom was restricted because of forecast high ash concentrations. The ash cloud was probably ~ 2 days old, but still contained quite high mass loadings. Research

aircraft and space-borne lidar measurements suggest that these clouds may have been as little as 300 m thick and up to 3 km thick in some parts [86], [87]. Hence the ash concentrations may vary by an order of magnitude within the same cloud. This very high ash cloud inhomogeneity makes forecasting safe levels very difficult and it seems desirable for commercial aircraft to carry on-board instrumentation capable of detecting ash clouds ahead of the aircraft.

Satellite remote sensing may also be used to measure ash fall deposits on land and, when used with a dispersion model, estimates of the amount of ash falling in to the ocean can also be made. The sensitivity of the ash retrievals in the infrared is restricted to particles in the size range of 1–16 μm radius: particle sizes that are thought to cause problems for jet engines and that also lie in the respirable range of particles that cause health related problems.

F. Remote sensing of SO_2

As can be seen from the panels in Fig. 10 it is possible to measure SO_2 column amount in the ultra-violet and in the infrared portions of the EM spectrum. The UV portion has been used since the discovery of anomalies in ozone retrievals from the Total Ozone Mapping Spectrometer (TOMS) due to SO_2 emissions during the 1982 El Chichon eruptions [88]. This led directly to the development of algorithms to determine SO_2 using TOMS and later to the incorporation of SO_2 channels into GOME, GOME-2, SCHIAMACHY, OMI and most recently OMPS (Ozone Mapping and Profiler Suite). Prata and colleagues [89] showed for the first time that infrared data from the operational meteorological HIRS (High Resolution infrared Sounder) sensor, part of the TIROS Operational Vertical Sounder (TOVS) package on the NOAA polar-orbiting satellites, could be used to determine upper troposphere/lower stratosphere SO_2 from volcanic activity. Further developments in infrared SO_2 retrievals have occurred using ASTER, MODIS, AIRS and IASI [90]. Fig. 17 shows a composite of AIRS SO_2 retrievals for the period 5–13 May, 2010, when Eyjafjallajökull was emitting SO_2 and ash. The retrieval scheme is insensitive to ash and SO_2 below approximately 3 km, so the SO_2 detected is in the mid-to-upper troposphere in a region of the atmosphere where aircraft fly. Because SO_2 is generally much easier to detect from satellites, some researchers have suggested that it may be used as surrogate detection for volcanic ash clouds. However, ash and SO_2 do not always travel together [91].

IV. LOOKING TO THE FUTURE

We have presented here some of the recent developments in the remote sensing of volcanic hazards and their precursors. Using InSAR, it is possible to measure surface displacements with an accuracy, in the best case, on the order of 1 mm/year over a few 10s of km. Until now, InSAR has principally been used as a tool for analysing deformation processes some time after the fact, but with the upcoming launch of the Sentinel-1 satellites by ESA planned in 2013, SAR data will be acquired for almost every point on Earth at least once every six days, at a similar resolution to that of Envisat. When taken together with data from other SAR satellites, this opens up the possibility of using InSAR for near-real time monitoring. The noise and other error sources present in interferograms will also continue to be addressed from a technological point of view in future missions. Decorrelation noise is reduced by acquiring images more frequently, increasing bandwidth and using a longer wavelength. Ionospheric phase delay can be estimated using a split-bandwidth system [92], [93], as it is frequency dependent, and tropospheric phase delay could be estimated using a system that simultaneously acquires data in a forward and backward looking direction. The accuracy of precise orbits continues to improve, as do elevation models, reducing residual geometric errors. A major drawback still, on many volcanoes, is the inability to make measurements on snow and ice, as well as in areas of heavy vegetation. Repeated DEM generation using, for example, the TanDEM-X constellation may provide a way to address this issue. Other possible approaches include the emplacement of active transponders in the incoherent areas, or the use of airborne SAR with very short revisit times.

Spectroradiometry has seen numerous advances and innovations over the period of 30 years since routine Earth observation began. There has been a trend towards higher spatial resolutions (0.5 m pixels are now possible), much greater spectral resolutions (1000's of channels on some hyper spectral instruments) and innovative measurement techniques introduced, such as multiple cameras for stereoscopic viewing, use of polarised light and limb scanning to improve vertical resolution. So far there has not been a satellite mission dedicated to volcanology and there are no missions planned in the next 20 years or so. However, there are numerous opportunities for volcanology to prosper by exploiting measurement synergies with other disciplines and by harnessing the interest in using space-based assets for natural hazards and crisis management. The new geostationary platforms MTG (Meteosat Third Generation) and the GOES-R (Geostationary

Operational Environmental Satellite) will provide a significant improvement in the capability to remotely sense volcanic hazards in a continuous manner over certain regions of the globe. MTG is a system of satellites that includes both imaging and sounding capability at UV, visible and infrared wavelengths. An interesting feature of MTG will be the lightning detector instrument (LI), which could be used to infer volcanic activity from the lightning generated. There will also be a Fourier Transform Interferometer, which will be able to sound the atmosphere at 0.625 cm^{-1} resolution, thus providing continuous measurements of ash and SO_2 . GOES-R is a geostationary platform designed to continuously image continental USA, and due for launch in 2015. The platform will carry the Geostationary Lightning Mapper (GLM) and the Advanced Baseline Imager (ABI) which can measure volcanic ash and height as well as infer column abundance of SO_2 . The proposed HySpri mission from NASA is an excellent example of how volcanologists can influence the choice of spectral channels, the spatial resolution and the repetition rate for a system that is still being planned. Volcanologists interested in gaseous and particle emissions from volcanoes to the atmosphere can also exploit synergies with atmospheric scientists interested in determining the composition of the atmosphere to better understand climate change. The OCO-2 mission will offer volcanologists the best opportunity to measure volcanic CO_2 from space over the next few years. The sporadic nature of volcanic activity, together with the remoteness and unpredictability of eruptions make remote sensing an indispensable tool for scientific investigation, early warning and monitoring; the future looks bright for spectroradiometric observations of volcanoes and their emissions.

Together InSAR and spectroradiometric observations are important space technology tools for modern monitoring of volcanic hazards and their precursors, and we expect their use to continue to grow in the future.

ACKNOWLEDGEMENTS

We thank Sebastiano Serpico for soliciting this review. ERS and Envisat data were provided by the European Space Agency (ESA). TerraSAR-X data were provided by the German Aerospace Centre (DLR). Some figures were prepared using the public-domain GMT software [94]. This work was partly supported by the University of Iceland Research Fund and the Icelandic Research Fund.

REFERENCES

- [1] C. Newhall, *Volcano Warnings*. San Diego Academic Press, 2000, pp. 1185–1197.
- [2] D. Dzurisin, *Volcano Deformation, New Geodetic Monitoring Techniques*. Springer-Praxis, 2006.
- [3] J. C. Curlander and R. N. McDonough, *Synthetic aperture radar - Systems and signal processing*. John Wiley & Sons, New York, 1991.
- [4] E. Magnússon, M. T. Gudmundsson, G. Sigurdsson, M. J. Roberts, F. Höskuldsson, and B. Oddsson, “Details of ice volcano interaction observed with airborne imaging radar during the 2010 Eyjafjallajökull eruption,” *J. Geophys. Res.*, in review.
- [5] R. Michel, J. Avouac, and J. Taboury, “Measuring ground displacements from SAR amplitude images: application to the Landers earthquake,” *Geophys. Res. Lett.*, vol. 26, no. 7, pp. 875–878, 1999.
- [6] T. J. Wright, C. Ebinger, J. Biggs, A. Ayele, G. Yirgu, D. Keir, and A. Stork, “Magma-maintained rift segmentation at continental rupture in the 2005 Afar dyking episode,” *Nature*, vol. 442, no. 7100, pp. 291–294, 2006.
- [7] P. Rosen, S. Hensley, I. Joughin, F. Li, S. Madsen, E. Rodriguez, and R. Goldstein, “Synthetic aperture radar interferometry,” *Proceedings of the IEEE*, vol. 88, no. 3, pp. 333–382, 2000.
- [8] R. F. Hanssen, *Radar Interferometry Data Interpretation and Error Analysis*. Springer, 2001.
- [9] C. W. Chen and H. A. Zebker, “Network approaches to two-dimensional phase unwrapping: intractability and two new algorithms,” *J. Opt. Soc. Am. A*, vol. 17, no. 3, pp. 401–414, 2000.
- [10] S. Hensley, H. Zebker, C. Jones, T. Michel, R. Muellerschoen, and B. Chapman, “First deformation results using the NASA/JPL UAVSAR instrument,” *2nd Asian-Pacific Conference on Synthetic Aperture Radar, Oct 2009*, pp. 1051–1055, 2009.
- [11] D. Massonnet, P. Briole, and A. Arnaud, “Etna monitored by spaceborne radar interferometry,” *Nature*, vol. 375, pp. 567–570, 1995.
- [12] D. Massonnet and F. Sigmundsson, “Remote sensing of volcano deformation by radar interferometry from various satellites,” in *Remote Sensing of Active Volcanism, Geophys. Monogr. Ser.*, 2000, vol. 116, pp. 207–221.
- [13] H. Zebker, F. Amelung, and S. Jonsson, “Remote sensing of volcano surface and internal processes using radar interferometry,” in *Remote Sensing of Active Volcanism, Geophys. Monogr. Ser.*, P. J. Mouginiis-Mark, J. A. Crisp, and J. H. Fink, Eds. American Geophysical Union, 2000, vol. 116, pp. 179–205.
- [14] Z. Lu, C. Wicks, D. Dzurisin, W. Thatcher, J. Freymueller, S. McNutt, and D. Mann, “Aseismic inflation of Westdahl volcano, Alaska, revealed by satellite radar interferometry,” *Geophys. Res. Lett.*, vol. 27, no. 11, pp. 1567–1570, 2000.
- [15] Y. Fialko and M. Simons, “Evidence for on-going inflation of the Socorro magma body, New Mexico, from Interferometric Synthetic Aperture Radar imaging,” *Geophys. Res. Lett.*, vol. 28, no. 18, pp. 3549–3552, 2001.
- [16] M. E. Pritchard and M. Simons, “A satellite geodetic survey of large-scale deformation of volcanic centres in the central Andes,” *Nature*, vol. 418, no. 6894, pp. 167–171, JUL 2002.
- [17] C. W. Wicks, W. Thatcher, D. Dzurisin, and J. Svarc, “Uplift, thermal unrest and magma intrusion at Yellowstone caldera,” *Nature*, vol. 440, no. 7080, pp. 72–75, 2006.
- [18] S. Jónsson, H. Zebker, P. Cervelli, P. Segall, H. Garbeil, P. Mouginiis-Mark, and S. Rowland, “A shallow-dipping dike fed the 1995 flank eruption at Fernandina volcano, Galapagos, observed by satellite radar interferometry,” *Geophys. Res. Lett.*, vol. 26, no. 8, pp. 1077–1080, 1999.
- [19] Y. Fukushima, V. Cayol, and P. Durand, “Finding realistic dike models from interferometric synthetic aperture radar data: The February 2000 eruption at Piton de la Fournaise,” *J. Geophys. Res.*, vol. 110, 2005.

- [20] R. Pedersen and F. Sigmundsson, "Temporal development of the 1999 intrusive episode in the Eyjafjallajökull volcano, Iceland, derived from InSAR images," *Bull. Volcanol.*, vol. 68, pp. 377–393, 2006.
- [21] F. Amelung, S. Jónsson, H. Zebker, and P. Segall, "Widespread uplift and 'trapdoor' faulting on Galapagos volcanoes observed with radar interferometry," *Nature*, vol. 407, no. 6807, pp. 993 – 996, 2000.
- [22] J. Froger, Y. Fukushima, P. Briole, T. Staudacher, T. Souriot, and N. Villeneuve, "The deformation field of the August 2003 eruption at Piton de la Fournaise, Reunion Island, mapped by ASAR interferometry," *Geophys. Res. Lett.*, vol. 31, no. 14, p. L14601, 2004.
- [23] S. Yun, H. Zebker, P. Segall, A. Hooper, and M. Poland, "Interferogram formation in the presence of complex and large deformation," *Geophys. Res. Lett.*, vol. 34, no. 12, p. L12305, 2007.
- [24] F. Sigmundsson, S. Hreinsdóttir, A. Hooper, T. Árnadóttir, R. Pedersen, M. J. Roberts, N. Óskarsson, A. Auriac, J. Decriem, P. Einarsson *et al.*, "Intrusion triggering of the 2010 Eyjafjallajökull explosive eruption," *Nature*, vol. 468, no. 7322, pp. 426–430, 2010.
- [25] D. Dzurisin and Z. Lu, "Interferometric Synthetic Aperture Radar (InSAR)," in *Volcano Deformation: Geodetic Monitoring Techniques*, D. Dzurisin, Ed. Springer-Praxis Publishing Ltd., 2007.
- [26] X. Zhu and R. Bamler, "Very high resolution spaceborne SAR Tomography in urban environment," *IEEE Trans. Geosci. Remote Sens.*, vol. 48, no. 12, pp. 4296–4308, 2010.
- [27] H. A. Zebker and J. Villasenor, "Decorrelation in interferometric radar echoes," *IEEE Trans. Geosci. Remote Sens.*, vol. 30, no. 5, pp. 950 – 9, 1992.
- [28] F. Gatelli, A. M. Guamieri, F. Parizzi, P. Pasquali, C. Prati, and F. Rocca, "The wavenumber shift in SAR interferometry," *IEEE Trans. Geosci. Remote Sens.*, vol. 32, no. 4, pp. 855 – 865, 1994.
- [29] R. M. Goldstein, H. A. Zebker, and C. L. Werner, "Satellite radar interferometry: two-dimensional phase unwrapping," *Radio Science*, vol. 23, no. 4, pp. 713 – 20, Jul-Aug 1988.
- [30] H. Zebker, P. Rosen, and S. Hensley, "Atmospheric effects in interferometric synthetic aperture radar surface deformation and topographic maps," *J. Geophys. Res.*, vol. 102, no. B4, pp. 7547–7563, 1997.
- [31] D. Perissin and A. Ferretti, "Urban-target recognition by means of repeated spaceborne SAR images," *IEEE Trans. Geosci. Remote Sens.*, vol. 45, no. 12, pp. 4043 –4058, 2007.
- [32] A. Ferretti, C. Prati, and F. Rocca, "Permanent scatterers in SAR interferometry," *IEEE Trans. Geosci. Remote Sens.*, vol. 39, no. 1, pp. 8 – 20, 2001.
- [33] B. M. Kampes, "Displacement parameter estimation using permanent scatterer interferometry," Ph.D. dissertation, Delft University of Technology, 2005.
- [34] A. Hooper, H. Zebker, P. Segall, and B. Kampes, "A new method for measuring deformation on volcanoes and other natural terrains using InSAR persistent scatterers," *Geophys. Res. Lett.*, vol. 31, no. 23, 2004.
- [35] M. van der Kooij, W. Hughes, S. Sato, and V. Poncos, "Coherent target monitoring at high spatial density: Examples of validation results," *European Space Agency, (Special Publication) ESA SP-610*, 2006.
- [36] A. Hooper, "A statistical-cost approach to unwrapping the phase of insar time series," *European Space Agency, (Special Publication) ESA SP-677*, 2010.
- [37] M. Doin, P. Lopez-Quiroz, Y. Yan, P. Bascou, and V. Pinel, "Time series analysis of Mexico City subsidence constrained by radar interferometry," *7th EGU General Assembly 2010, Vienna*, vol. 12, pp. EGU2010–12 031, 2010.
- [38] J. J. Sousa, A. J. Hooper, R. F. Hanssen, L. C. Bastos, and A. M. Ruiz, "Persistent Scatterer InSAR: A comparison of

- methodologies based on a model of temporal deformation vs. spatial correlation selection criteria,” *Remote Sens. Env.*, vol. 115, no. 10, pp. 2652 – 2663, 2011.
- [39] P. Berardino, G. Fornaro, R. Lanari, and E. Sansosti, “A new algorithm for surface deformation monitoring based on small baseline differential SAR interferograms,” *IEEE Trans. Geosci. Remote Sens.*, vol. 40, no. 11, pp. 2375 – 83, 2002.
- [40] D. A. Schmidt and R. Bürgmann, “Time-dependent land uplift and subsidence in the Santa Clara valley, California, from a large interferometric synthetic aperture radar data set,” *J. Geophys. Res.*, vol. 108, no. B9, pp. 2416 – 28, 2003.
- [41] G. Fornaro, A. Pauciuolo, and F. Serafino, “Deformation monitoring over large areas with multipass differential SAR interferometry: A new approach based on the use of spatial differences,” *Int. J. Rem. Sens.*, vol. 30, no. 6, pp. 1455–1478, 2009.
- [42] R. Lanari, O. Mora, M. Manunta, J. J. Mallorqui, P. Berardino, and E. Sansosti, “A small-baseline approach for investigating deformations on full-resolution differential SAR interferograms,” *IEEE Trans. Geosci. Remote Sens.*, vol. 42, no. 7, pp. 1377–1386, 2004.
- [43] A. Hooper, “A multi-temporal InSAR method incorporating both persistent scatterer and small baseline approaches,” *Geophys. Res. Lett.*, vol. 35, p. L16302, 2008.
- [44] F. K. Li and R. M. Goldstein, “Studies of multibaseline spaceborne interferometric synthetic aperture radars,” *IEEE Trans. Geosci. Remote Sens.*, vol. 28, no. 1, pp. 88 – 97, Jan 1990.
- [45] A. Pepe and R. Lanari, “On the extension of the minimum cost flow algorithm for phase unwrapping of multitemporal differential SAR interferograms,” *IEEE Trans. Geosci. Remote Sens.*, vol. 44, no. 9, pp. 2374–2383, 2006.
- [46] T. Lauknes, H. Zebker, and Y. Larsen, “InSAR deformation time series using an L_1 -Norm small-baseline approach,” *IEEE Trans. Geosci. Remote Sens.*, vol. 49, no. 1, pp. 536 –546, jan 2011.
- [47] J. Biggs, T. Wright, Z. Lu, and B. Parsons, “Multi-interferogram method for measuring interseismic deformation: Denali fault, Alaska,” *Geophys. J. Int.*, vol. 170, pp. 1165–1179, 2007.
- [48] A. Ferretti, A. Fumagalli, F. Novali, C. Prati, F. Rocca, and A. Rucci, “A new algorithm for processing interferometric data-stacks: SqueeSAR,” *IEEE Trans. Geosci. Remote Sens.*, vol. 49, no. 9, pp. 3460–3470, 2011.
- [49] A. Hooper, R. Pedersen, and F. Sigmundsson, “Constraints on magma intrusion at Eyjafjallajökull and Katla volcanoes in Iceland, from time series SAR interferometry,” in *VOLUME Project Volcanoes: Understanding Subsurface Mass Movement*, C. J. Bean *et al.*, Eds. University College Dublin, 2009, pp. 13–24.
- [50] B. Ofeigsson, A. Hooper, F. Sigmundsson, E. Sturkell, and R. Grapenthin, “Deep magma storage at Hekla volcano, Iceland, revealed by InSAR time series analysis,” *J. Geophys. Res.*, vol. 116, no. B5, p. B05401, 2011.
- [51] S. Liu, R. Hanssen, and A. Mika, “On the value of high-resolution weather models for atmospheric mitigation in SAR interferometry,” *2009 IEEE Int. Geosci and Remote Sensing Symposium (IGARSS)*, vol. 45, no. 12, pp. 4043–4058, 2009.
- [52] C. Wicks, D. Dzurisin, S. Ingebritsen, W. Thatcher, Z. Lu, and J. Iverson, “Magmatic activity beneath the quiescent Three Sisters volcanic center, central Oregon Cascade Range, USA,” *Geophys. Res. Lett.*, vol. 29, no. 7, pp. 26–1, 2002.
- [53] G. Wadge, P. W. Webley, I. N. James, R. Bingley, A. Dodson, S. Waugh, T. Veneboer, G. Puglisi, M. Mattia, D. Baker, S. C. Edwards, S. J. Edwards, and P. J. Clarke, “Atmospheric models, GPS and InSAR measurements of the tropospheric water vapour field over Mount Etna,” *Geophys. Res. Lett.*, vol. 29, no. 19, 2002.
- [54] S. Williams, Y. Bock, and P. Fang, “Integrated satellite interferometry: Tropospheric noise, GPS estimates and implications for interferometric synthetic aperture radar products,” *J. Geophys. Res.*, vol. 103, 1998.
- [55] B. Puysségur, R. Michel, and J. Avouac, “Tropospheric phase delay in interferometric synthetic aperture radar estimated from meteorological model and multispectral imagery,” *J. Geophys. Res.*, vol. 112, p. B05419, 2007.

- [56] Z. Li, P. Fielding, E. J. Cross, and R. Preusker, "Advanced InSAR atmospheric correction: MERIS/MODIS combination and stacked water vapour models," *Int. J. of Rem. Sensing*, vol. 30, no. 13, pp. 3343–3363, 2009.
- [57] V. Pinel, A. Hooper, S. De la Cruz-Reyna, G. Reyes-Davila, and M. P. Doin, "The challenging retrieval of displacement field from InSAR data for andesitic stratovolcanoes: Case study of Popocatepetl and Colima Volcano, Mexico," *J. Volc. Geotherm. Res.*, vol. 200, no. 1-2, pp. 49–61, 2011.
- [58] A. N. Rencz, Ed., *Manual of Remote Sensing, Volume 3, Remote Sensing for the Earth Sciences*, 3rd ed. Wiley & Sons, Inc., 1999.
- [59] T. R. Lillesand, W. Kiefer, and J. Chipman, *Remote sensing and image interpretation*, 6th ed. Wiley & Sons Inc., 2008.
- [60] K. N. Liou, *An introduction to atmospheric radiation*. Academic Press, Elsevier Science (USA), 2002.
- [61] N. Krotkov, S. A. Carn, A. J. Krueger, P. K. Bhartia, and K. Yang, "Band residual difference algorithm for retrieval of SO_2 from the Aura ozone monitoring instrument (omi)," *IEEE Trans. Geosci. Rem. Sensing*, vol. 44, no. 5, pp. 1259–1266, 2006.
- [62] J. T. Houghton, F. W. Taylor, and C. D. Rodgers, *Remote Sounding of Atmospheres*. Cambridge University Press, London, 1984.
- [63] C. D. Rodgers, *Inverse Methods for Atmospheric Sounding: Theory and Practice*. World Scientific Publishing Co. Ltd., 2000.
- [64] A. J. Prata and I. F. Grant, "Retrieval of microphysical and morphological properties of volcanic ash plumes from satellite data: Application to Mt. Ruapehu, New Zealand," *Quart. J. Roy. Meteorol. Soc.*, vol. 127, no. 576B, pp. 2153–2179, 2001.
- [65] D. A. Rothery, M. Coltelli, D. Pirie, M. J. Wooster, and R. Wright, "Documenting surface magmatic activity at Mount Etna using ATSR remote sensing," *Bull. Volc.*, vol. 63, pp. 387–397, 2001.
- [66] A. J. L. Harris, L. P. Flynn, K. Dean, E. Pilger, M. Wooster, C. Okubo, P. Mougini-Mark, H. Garbeil, C. Thornber, S. D. la Cruz-Reyna, D. Rothery, and R. Wright, "Real-time satellite monitoring of volcanic hot spots," in *Remote Sensing of Active Volcanism, Geophys. Monogr. Ser.*, P. J. Mougini-Mark, J. A. Crisp, and J. H. Fink, Eds. American Geophysical Union, 2000, vol. 116, pp. 139–15.
- [67] M. J. Wooster and D. A. Rothery, *A Review of Volcano Surveillance Applications Using the ATSR Instrument Series*, 2000, vol. 1, no. 1, pp. 3–35.
- [68] R. Wright, L. P. Flynn, H. Garbeil, A. J. L. Harris, and E. Pilger, "MODVOLC: Near-real-time thermal monitoring of global volcanism," *J. Volc. Geotherm. Res.*, vol. 135, pp. 29–49, 2004.
- [69] A. J. Carter and M. S. Ramsey, "ASTER- and field-based observations at Bezymianny Volcano: Focus on the 11 May 2007 pyroclastic flow deposit," *Rem. Sens. Environ.*, vol. 113, pp. 2142–2151, 2009.
- [70] D. A. Rothery, D. Coppola, and C. Saunders, "Analysis of volcanic activity patterns using MODIS thermal alerts, *bull.*" *Bull. Volc.*, vol. 67, pp. 539–556, 2005.
- [71] M. S. Ramsey and L. P. Flynn, "Strategies, insights, and the recent advances in volcanic monitoring and mapping with data from NASA's Earth Observing System," *J. Volc. Geotherm. Res.*, vol. 135, no. 1–2, pp. 1–11, 2004.
- [72] D. Pieri and S. Baloga, "Eruption rate, area, and length relationships for some Hawaiian lava flows," *J. Volcanol. Geotherm. Res.*, vol. 30, pp. 29–45, 1986.
- [73] R. Wright, S. Blake, A. J. L. Harris, and D. A. Rothery, "A simple explanation for the space-based calculation of lava eruption rates," *Earth Planet. Sci. Lett.*, vol. 192, pp. 223–233, 2001.
- [74] R. Wright, L. Flynn, H. Garbeil, A. Harris, and E. Pilger, "Automated volcanic eruption detection using MODIS," *Rem. Sens. Environ.*, vol. 82, no. 1, pp. 135–155, 2002.

- [75] F. Marchese, C. Filizzola, N. Genzano, G. Mazzeo, N. Pergola, and V. Tramutoli, "Assessment and improvement of a robust satellite technique (RST) for thermal monitoring of volcanoes," *Rem. Sens. Env.*, vol. 115, pp. 1556–1563, 2011.
- [76] W. Koeppen, E. Pilger, and R. Wright, "Time series analysis of infrared satellite data for detecting thermal anomalies: a hybrid approach," *Bull. Volc.*, vol. 73, no. 5, pp. 577–593, 2011.
- [77] C. Oppenheimer, "Lava flow cooling estimated from landsat thematic mapper infrared data: the lonquimay eruption (chile, 1989)," *J. Geophys. Res.*, vol. 96, no. B13, pp. 21 865–21 878,, 1991.
- [78] D. A. Rothery, P. W. Francis, and C. A. Wood, "Volcano monitoring using short wavelength infrared data from satellites," *J. Geophys. Res.*, vol. 93, no. B7, pp. 7993–8008, 1988.
- [79] A. J. L. Harris, S. Blake, and D. A. Rothery, "A chronology of the 1991 to 1993 Mount Etna eruption using Advanced Very High Resolution Radiometer data: Implications for real-time thermal volcano monitoring," *J. Geophys. Res.*, vol. 102, no. B4, pp. 7985–8003, 1997.
- [80] T. J. Casadevall, P. J. D. Reyes, and D. J. Schneider, "The 1991 pinatubo eruptions and their effects on aircraft operations," in *Fire and Mud: Eruptions and Lahars of Mount Pinatubo, Philippines*, C. Newhall and R. S. Punongbayan, Eds. Quezon City: University of Washington Press, Seattle, 1996, pp. 625–636.
- [81] A. J. Prata, "Radiative transfer calculations for volcanic ash clouds," *Geophys. Res. Lett.*, vol. 16, no. 11, pp. 1293–1296, 1989.
- [82] M. T. Chahine, T. S. Pagano, H. H. Aumann *et al.*, "AIRS: Improving weather forecasting and providing new data on greenhouse gases," *Bull. Amer. Meteorol. Soc.*, pp. 910–926, 2006.
- [83] A. J. Prata and A. T. Prata, "Eyjafjallajökull volcanic ash concentrations determined using Spin Enhanced Visible and Infrared Imager measurements," *J. Geophys. Res.*, vol. 117, p. D00U23, 2012.
- [84] L. G. Mastin, M. Guffanti, R. Servranckx, P. Webley, S. Barsotti, K. Dean, A. Durant, J. W. Ewert, A. Neri, W. I. Rose, D. Schneider, L. Siebert, B. Stunder, G. Swanson, A. Tupper, A. Volentik, and C. F. Waythomas, "A multidisciplinary effort to assign realistic source parameters to models of volcanic ash-cloud transport and dispersion during eruptions," *J. Volc. Geothermal Res.*, vol. 86, no. 1–2, pp. 10–21, 2009.
- [85] A. Stohl, A. J. Prata, S. Eckhardt, L. Clarisse, A. Durant, S. Henne, N. I. Kristiansen, A. Minikin, U. Schumann, P. Seibert, K. Stebel, H. E. Thomas, T. Thorsteinsson, K. Trseth, and B. Weinzierl, "Determination of time- and height-resolved volcanic ash emissions and their use for quantitative ash dispersion modeling: the 2010 Eyjafjallajökull eruption," *Atmos. Chem. Phys.*, vol. 11, pp. 4333–4351, 2011.
- [86] D. M. Winker, Z. Liu, A. Omar, J. Tackett, and D. Fairlie, "CALIOP observations of the transport of ash from the Eyjafjallajökull volcano in April 2010," *J. Geophys. Res.*, vol. 117, p. D00U15, 2012.
- [87] F. Marengo, B. Johnson, K. Turnbull, S. Newman, J. Haywood, H. Webster, and H. Ricketts, "Airborne lidar observations of the 2010 Eyjafjallajökull volcanic ash plume," *J. Geophys. Res.*, vol. 116, p. D00U05, 2011.
- [88] A. J. Krueger, "Sighting of El Chichon sulfur dioxide clouds with the Nimbus 7 Total Ozone Mapping Spectrometer," *Science*, vol. 220, pp. 1377–1378, 1983.
- [89] A. J. Prata, W. I. Rose, S. Self, and D. M. O'Brien, "Global, long-term sulphur dioxide measurements from TOVS data: A new tool for studying explosive volcanism and climate," in *Volcanism and the Earth's Atmosphere, Geophys. Monogr. Ser.* American Geophysical Union, 2003, vol. 139, pp. 75–92.
- [90] A. J. Prata, G. J. S. Bluth, S. A. Carn, V. J. Realmuto, and I. M. Watson, "Gas emissions from volcanoes," in *Volcanoes of the North Pacific*, K. Dean and J. Dehn, Eds., 2012, in press.
- [91] H. E. Thomas and A. J. Prata, "Sulphur dioxide as a volcanic ash proxy during the april-may 2010 eruption of

- eyjafjallajökull volcano, iceland,” *Atmos. Chem. Phys.*, vol. 112011, pp. 6871–6880, 2010.
- [92] R. Brcic, A. Parizzi, M. Eineder, R. Bamler, and F. Meyer, “Estimation and compensation of ionospheric delay for SAR interferometry,” *2010 IEEE Int. Geosci. and Remote Sensing Symposium (IGARSS)*, pp. 2908–2911, 2010.
- [93] P. Rosen, S. Hensley, and C. Chen, “Measurement and mitigation of the ionosphere in L-band interferometric SAR data,” *2010 IEEE Radar Conference*, pp. 1459–1463, 2010.
- [94] P. Wessel and W. H. F. Smith, “New, improved version of the generic mapping tools released,” *EOS Trans. AGU*, vol. 79, p. 579, 1998.
- [95] A. Hooper, B. Ófeigsson, F. Sigmundsson, B. Lund, P. Einarsson, H. Geirsson, and E. Sturkell, “Increased capture of magma in the crust promoted by ice-cap retreat in Iceland,” *Nature Geosci.*, vol. 4, no. 11, pp. 783–786, 2011.
- [96] A. Bonforte, F. Guglielmino, M. Coltelli, A. Ferretti, and G. Puglisi, “Structural assessment of Mount Etna volcano from Permanent Scatterers analysis,” *Geochem. Geophys. Geosyst.*, vol. 12, no. 2, p. Q02002, 2011.
- [97] E. Trasatti, F. Casu, C. Giunchi, S. Pepe, G. Solaro, S. Tagliaventi, P. Berardino, M. Manzo, A. Pepe, G. P. Ricciardi *et al.*, “The 2004–2006 uplift episode at Campi Flegrei caldera (Italy): Constraints from SBAS-DInSAR ENVISAT data and Bayesian source inference,” *Geophys. Res. Lett.*, vol. 35, no. 7, p. L07, 2008.



Andrew Hooper was educated at Oxford University (B.A., Geology) and Stanford University (M.S., Geophysics). He went on to also receive his Ph.D. from Stanford in 2006, for his development of SAR persistent scatterer interferometry algorithms. Between 2002 and 2003, he worked at the German Space Center (DLR), Oberpfaffenhofen, Germany, on Doppler centroid determination for the TerraSAR-X satellite. From 2006 to 2008, he was a Research Scientist at the University of Iceland, Reykjavik, Iceland, developing more general SAR interferometry time series algorithms and applying them to model deformation at Icelandic volcanoes. Since 2008, he is Assistant Professor at Delft University of Technology, Delft, The Netherlands. His current research interests include imaging and modeling magma movement at volcanoes, slip on faults, and the solid Earth response to retreating glaciers.



Fred Prata is an expert in remote sensing of the Earth and atmosphere and specialises in the use of high-spectral resolution infrared measurements to understand natural hazards, including the fate and dispersion of volcanic ash in the atmosphere. Educated at Imperial College (B. Sc., Physics) and Oxford (D. Phil, Atmospheric Physics), Dr Prata emigrated to Australia in 1985 to join CSIRO. After 20 years he returned to Europe and is now a Senior Scientist at the Norwegian Institute for Air Research in Kjeller, Norway. Dr Prata is an Adjunct Professor at Michigan Technological University, USA and the Technical Director of Nicarnica AS, a private company developing imaging camera technology for use in measuring polluting gases and particulates. He has published over 100 papers in the peer reviewed literature and authored four patents.



Freysteinn Sigmundsson finished a M.S. degree from the University of Iceland, and a Ph.D. degree from the University of Colorado at Boulder in 1992. Then he joined the Nordic Volcanological Institute and was its director from 1999-2004, until it merged with University of Iceland. He is now a research scientist at the Nordic Volcanological Center, Institute of Earth Sciences, University of Iceland. He has been involved in various crustal deformation studies, utilizing both GPS-geodesy and satellite radar interferometry, and involved in the response to recent eruptions in Iceland. In particular, he has been working on effects of ice retreat on the solid Earth, and deformation processes taking place at the many volcanoes Iceland; with numerous publications of research results.

Mission	Period of operation	Wavelength	Orbit repeat time
SEASAT	Jun-Oct 1978	23.5 cm	17 days
ERS-1	Jul 1991 to Mar 2000	5.66 cm	3 or 35 days
ERS-2	Apr 1995 to Sep 2011	5.66 cm	3 or 35 days
JERS-1	Feb 1992 to Oct 1998	23.5 cm	44 days
SIR-C/X-SAR	9 to 20 Apr and 30 Sep to 11 Oct 1994	24.0, 5.66 and 3.1 cm	N/A
RADARSAT-1	Nov 1995 to present	5.6 cm	24 days
SRTM	11-22 Feb 2000	5.8 and 3.1 cm	N/A
Envisat	Mar 2002 to present ¹	5.63 cm	35 days ¹
ALOS	Jan 2006 to Apr 2011	23.5 cm	46 days
COSMO-SkyMed	Jun 2007 to present	3.1 cm	16 days
(constellation of	Dec 2007 to present	3.1 cm	16 days
4 satellites)	Oct 2008 to present	3.1 cm	16 days
	Nov 2010 to present	3.1 cm	16 days
TerraSAR-X	Jun 2007 to present	3.1 cm	11 days
TanDEM-X	Jun 2010 to present	3.1 cm	11 days
RADARSAT-2	Dec 2007 to present	5.6 cm	24 days

TABLE I

PAST AND PRESENT SIDE-LOOKING SAR SATELLITE MISSIONS (AS OF NOVEMBER 1, 2011)

¹Since November 2010, Envisat is operating in a new 30 day orbit, which is not optimal for interferometry at high latitudes.

Satellite platform	Launch date	Sensor/ Technology	Spatial resolution	Sampling frequency (d ⁻¹)	Main application
Landsat-1	23.07.1972	Whiskbroom imaging	80 m	1/16	Mapping
NOAA	26.06.1979 ¹	AVHRR Multi-spectral	1 km	4	Meteorology
Landsat-5	01.03.1984	Mid-range IR imaging	30–120 m	1/16	Mapping
SPOT-1	22.02.1986	Pushbroom imaging	10–30 m	1/16	Crises
Earlybird	24.12.1997	1st commercial imaging	1 m	1/16	Crises
Landsat-7	15.04.1999	Opto-mechanical, whiskbroom	0.03–0.12	1/16	Mapping
IKONOS-2	24.09.1999	1 m spatial resolution commercial imagery	1 m	On demand	Crises
Quickbird-2	18.10.2001	Commercial imagery	1 m	On demand	Crises
Terra	18.12.2001	MODIS/ASTER Earth observers	0.25–1 km	2	Hot-spots, ash, SO ₂
Aqua	04.05.2002	MODIS/AIRS Earth observers	0.25–14 km	2	Hot-spots, ash, SO ₂
IKONOS-2	24.09.2004	0.5 m spatial resolution commercial imagery	0.5 m	on demand	Crises
MSG-2	21.12.2005	SEVIRI 15 min multispectral imagery	1–4 km	96	Hot-spots, ash, SO ₂
MetOp	19.10.2006	IASI High-spectral resolution IR interferometer	10 km	2	Ash, SO ₂

TABLE II

HISTORICAL HIGHLIGHTS IN SPECTRORADIOMETRIC IMAGING OF THE EARTH AND ATMOSPHERE.

¹Date of first launch.¹Signal-to-Noise Ratio.²Noise-equivalent temperature difference

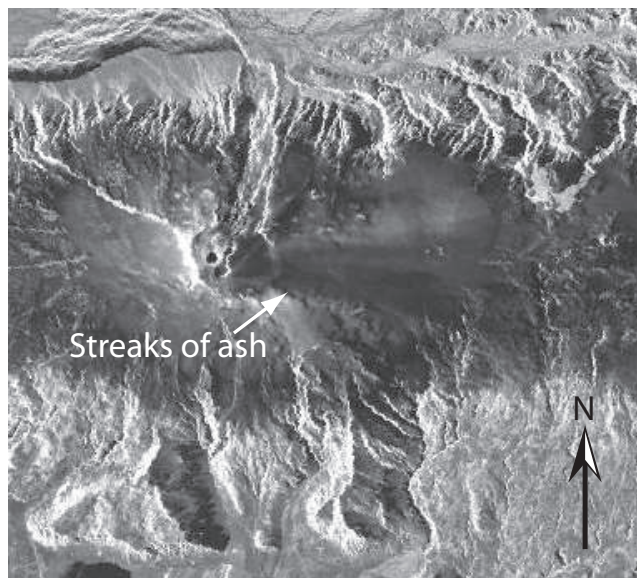


Fig. 1. A SAR amplitude image of Eyjafjallajökull volcano, Iceland. This image was acquired by the TerraSAR-X satellite on April 15, 2010, one day after an explosive eruption began. Three dark craters are clearly visible within the central caldera, and streaks of ash can be observed radiating to the east. The larger dark region represents the area covered by snow.

Primary Use (Reflective)	Band	Bandwidth (μm)	Required SNR ¹
Land/Cloud/Aerosols	1	620–670	128
Boundaries	2	841–876	201
Land/Cloud/Aerosols	3	459–479	243
Properties	4	545–565	228
	5	1230–1250	74
	6	1628–1652	275
	7	2105–2155	110
Ocean Color/	8	405–420	880
Phytoplankton/	9	438–448	838
Biogeochemistry	10	483–493	802
	11	526–536	754
	12	546–556	750
	13	662–672	910
	14	673–683	1087
	15	743–753	586
	16	862–877	516
Atmospheric	17	890–920	167
Water Vapor	18	931–941	57
	19	915–965	250
Primary Use (Emissive)	Band	Bandwidth (μm)	Radiance required $\text{NE}\Delta\text{T}^2$ (K)
Surface/Cloud	20	3.660–3.840	0.05
Temperature	21	3.929–3.989	2.00
	22	3.929–3.989	0.07
	23	4.020–4.080	0.07
Atmospheric	24	4.433–4.498	0.25
Temperature	25	4.482–4.549	0.25
Cirrus Clouds	26	1.360–1.390	150(SNR)
Water Vapor	27	6.535–6.895	0.25
	28	7.175–7.475	0.25
Cloud Properties	29	8.400–8.700	0.05
Ozone	30	9.580–9.880	0.25
Surface/Cloud	31	10.780–11.280	0.05
Temperature	32	11.770–12.270	0.05
Cloud Top	33	13.185–13.485	0.25
Altitude	34	13.485–13.785	0.25
	35	13.785–14.085	0.25
	36	14.085–14.385	0.35

TABLE III

TECHNICAL SPECIFICATIONS OF THE MODIS INSTRUMENT ABOARD NASA'S TERRA AND AQUA POLAR-ORBITING PLATFORMS. FOR THE SHORTWAVE REFLECTIVE CHANNELS THE NOISE REQUIREMENT IS GIVEN AS A SIGNAL-TO-NOISE RATIO; FOR THE THERMAL EMISSIVE CHANNELS THE NOISE REQUIREMENT IS SPECIFIED AS THE NOISE EQUIVALENT TEMPERATURE DIFFERENCE ($\text{NE}\Delta\text{T}$). (ADAPTED FROM [HTTP://MODIS.GSFC.NASA.GOV/ABOUT/SPECIFICATIONS.PHP](http://modis.gsfc.nasa.gov/about/specifications.php)).

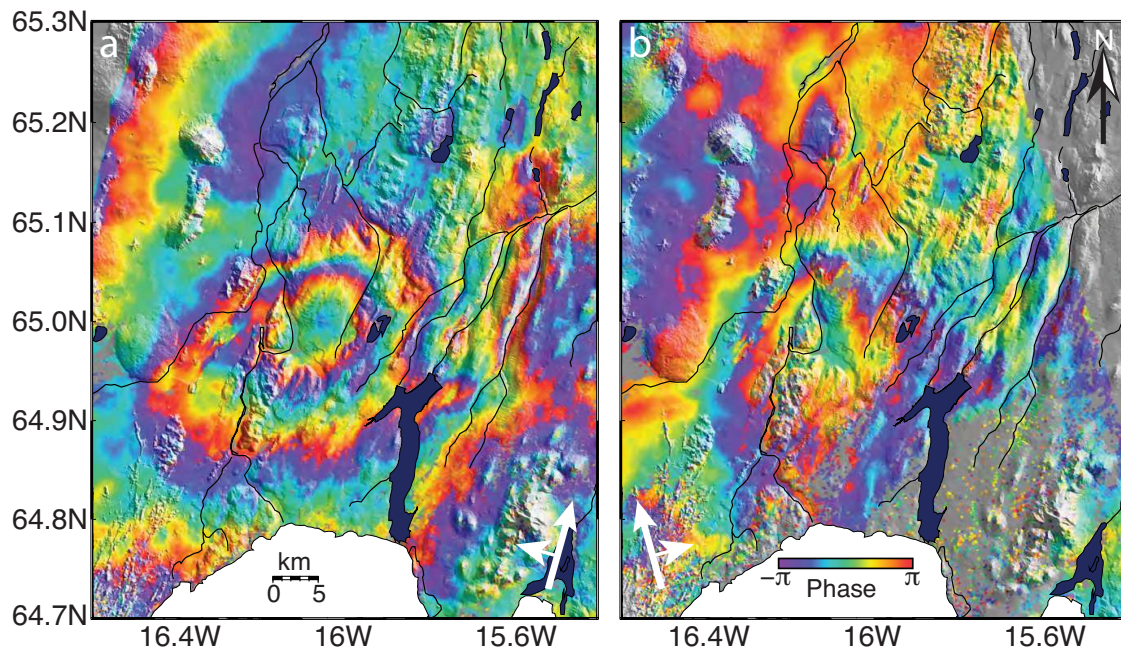


Fig. 2. Example interferograms displaying deformation between 2007 and 2008 due to the intrusion of a dike in the Northern Volcanic Zone north of the Vatnajökull ice cap (white area). The SAR data were acquired by the C-band Envisat satellite. Each color cycle represents 2.8 cm of displacement away from the satellite. In (a) the image spans July 14, 2007 to June 28, 2008 and in (b) the image spans June 27, 2007 to July 16, 2008. In both cases the direction of satellite motion is shown by the long white arrow and the look direction is shown by the short arrow. The same deformation is imaged in both interferograms, but the different look directions lead to a difference in the deformation pattern. The dike was emplaced between approximately 10 and 20 km depth, has a strike of 81 to 82° and is tilted, dipping approximately to the south by 42 to 43°. The intruded volume is estimated to be 42-47 million m³ [95].

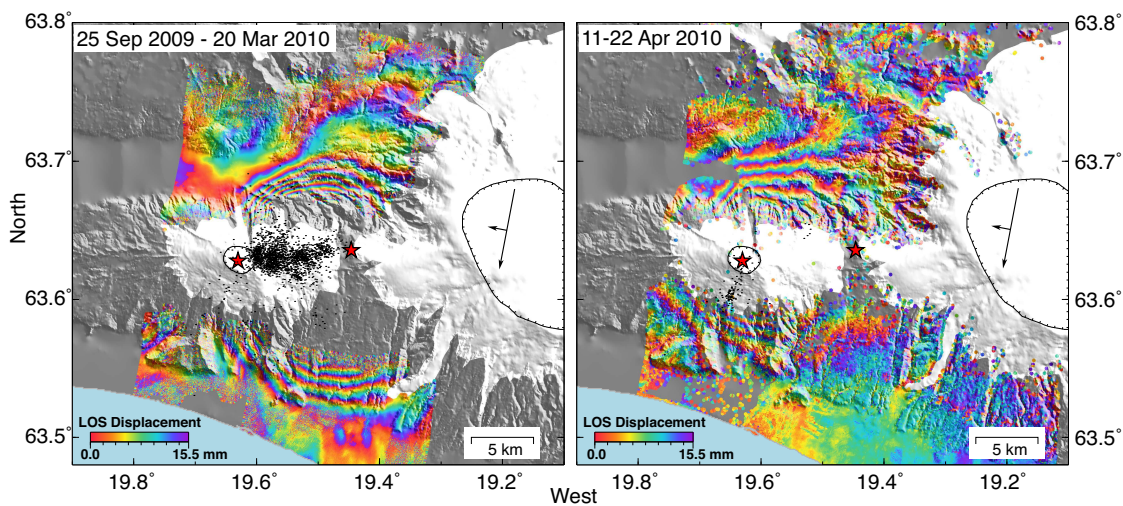


Fig. 3. Interferograms for the 2010 eruption of Eyjafjallajökull (from [24]). The data were acquired by the TerraSAR-X satellite from a descending satellite orbit. Interferogram (a) spans the pre-eruptive intrusive period and shows inflation due to a complex intrusion modeled as two sills at 4-6 km depth and a dike extending from this depth to the surface. Interferogram (b) spans the first eight days of the explosive eruption and shows deflation due to the depressurization of a magma body at 4-5 km depth. Black orthogonal arrows show the satellite flight path and look direction. One color fringe corresponds to a line-of-sight change of 15.5 mm (positive for increasing range, that is, motion of the ground away from the satellite). Black dots show earthquake epicenters for the corresponding period. Background is shaded topography. Red stars show the two eruptive sites and yellow triangles indicate locations of GPS stations.

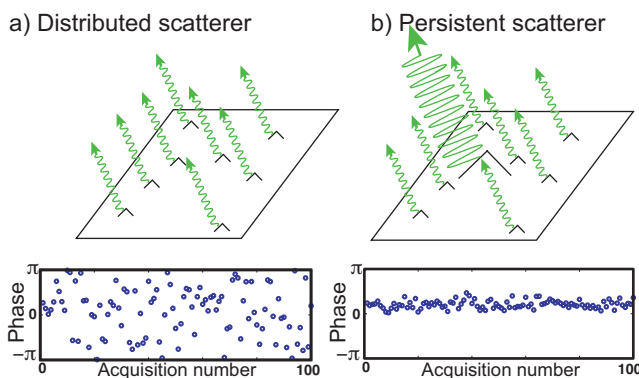


Fig. 4. Phase simulations for a distributed scatterer pixel and a persistent scatterer pixel. The cartoons above represent the scatterers contributing to the phase of one pixel in an image and the plots below show simulations of the phase for 100 acquisitions, with the smaller scatterers moving randomly between each iteration. The brighter scatterer in the persistent scatterer case has constant phase and an amplitude that is three times brighter than the sum of the smaller scatterers, which have random phase.

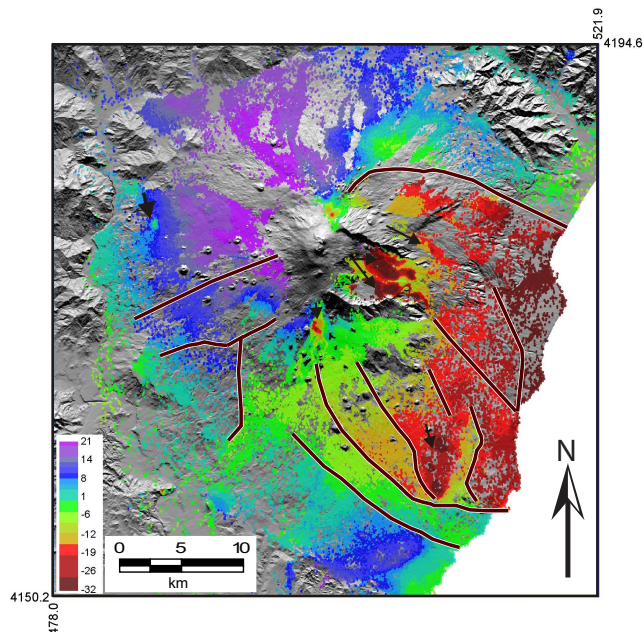


Fig. 5. Line-of-sight velocity map (mm/yr) for Mount Etna during 1995 to 2000 from persistent scatterer InSAR (modified after [96]). Data were acquired by ERS in an ascending orbit and processed with the method of Ferretti et al. [32]. The ground motion reveals that deformation of Mount Etna is characterized by two main domains. The first domain involves the entire western and northern flanks of the volcano and its summit area, undergoing fairly continuous inflation. The second domain involves the eastern and southern flanks of the volcano and is characterized by general eastward and downward motion at 1 to 3 cm/yr. This domain is divided into a number of blocks with slightly different velocities. Local areas of subsidence are visible near the summit due to cooling lava flows.

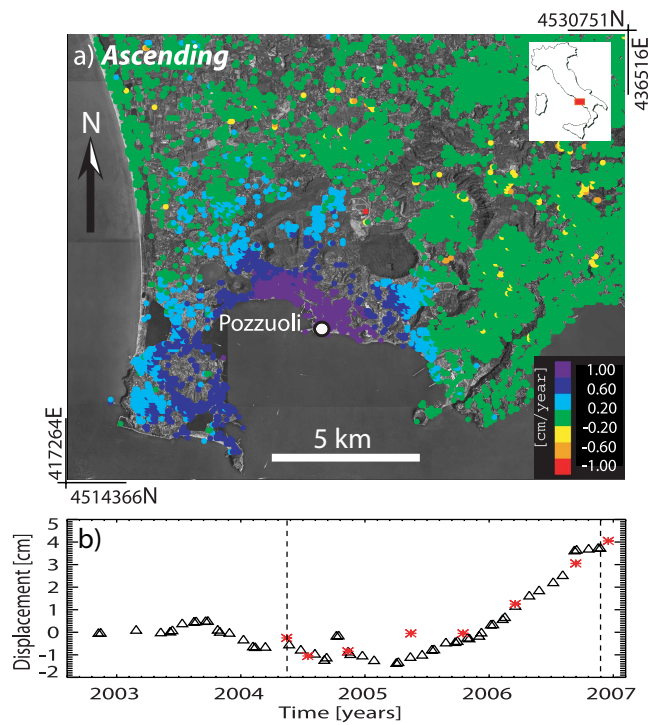


Fig. 6. Small baseline results for Campi Flegrei 2003-2006 from Envisat images (modified from [97]). (a) Mean LOS velocity map between summer 2004 and November 2006, superimposed on an orthophoto of the Campi Flegrei caldera. (b) Vertical displacement time series for the location identified by the white circle in (a). Black triangles indicate InSAR measurements and red stars indicate leveling measurements. The time interval spanned by (a) is indicated by the dashed lines. Inflation of the caldera is shown to accelerate during this interval.

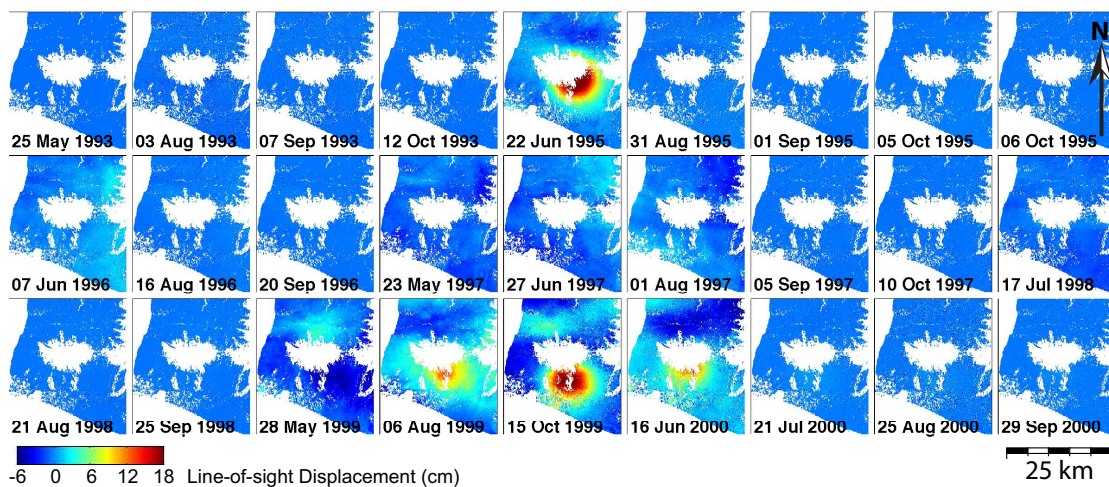


Fig. 7. Time series of displacement maps for Eyjafjallajökull volcano (from [49]). SAR data acquired by ERS between 1993 and 2000 were processed using the combined time series method of Hooper [43]. Each image shows the incremental LOS displacement since the date of the previous image. The white patch in the middle of each image with no scatterers is the ice cap. Two periods of deformation are visible, the first occurred in 1994 (visible in the image labelled 22 Jun 1995, which spans October 1993 to June 1995) and the second in 1999–2000. Both events can be modelled by the intrusion of a sill at 5–6 km depth, although the spatial extent varies for each event.

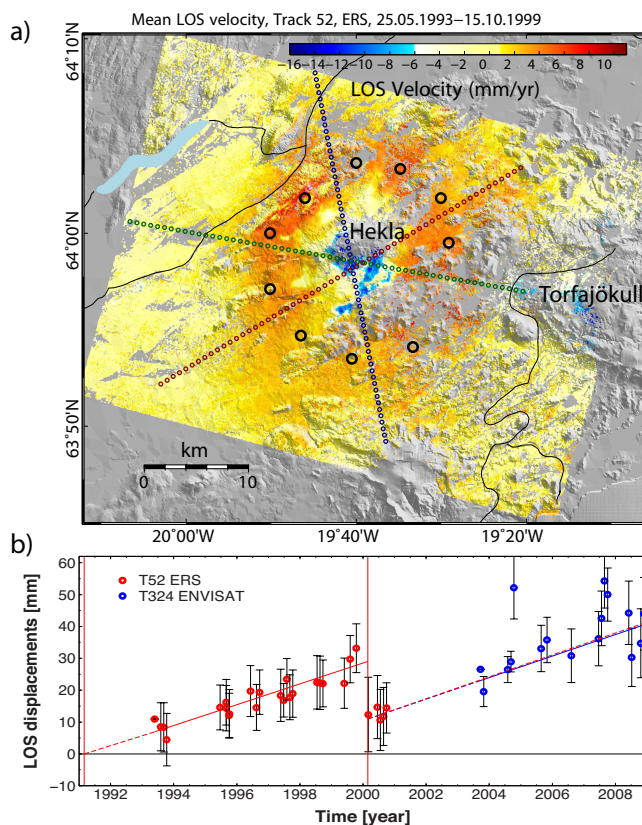


Fig. 8. Time series results for Hekla volcano (modified from [50]). (a) Mean LOS velocities before the 2000 eruption using data acquired by the ERS satellites from a descending orbit. A minus sign on the scale bar represents lengthening of LOS range. The deformation around Hekla is torus-like, with uplift rates increasing as one moves towards the summit, peaking at around 6 km from the summit (indicated by the black circles) and then decreasing again until eventually becoming subsidence. A second center of subsidence is observed east of Hekla, at Torfajökull. (b) A time series of the mean LOS displacement for the areas enclosed by the black circles in (a), from ERS (red circles) and Envisat (blue circles) satellites related to pressure changes in a deep magma chamber. The red vertical lines show the beginning of the January 17, 1991 and February 26, 2000 eruptions. Before the 2000 eruption, a steady rate of 3.3 ± 0.7 mm/yr in the LOS is inferred. A similar rate of 3.4 ± 2.0 mm/yr is inferred after the eruption (blue line). The dotted red line is a continuation of the fit for the ERS data (1993-1999) with an offset of -17 mm in the LOS occurring as a result of the 2000 eruption, caused by a co-eruptive pressure drop in the Hekla magma chamber.

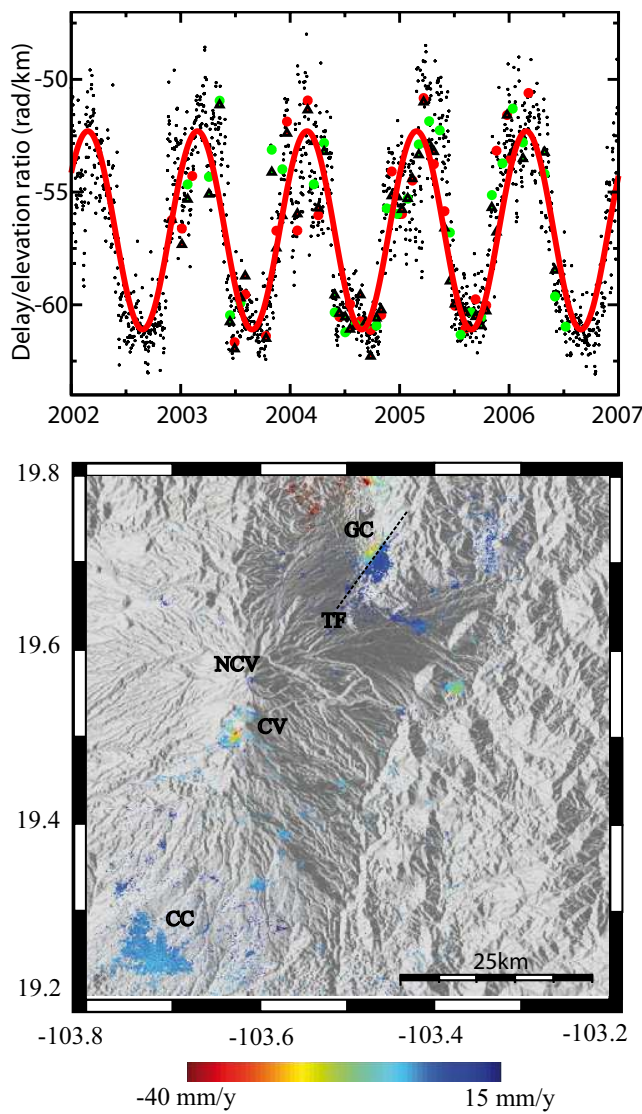


Fig. 9. Time series analysis for Colima Volcano (modified from [57]). Above, temporal evolution of the phase delay/elevation ratio (in rad/km) induced by the troposphere. Black dots represent the daily values calculated from the NARR global weather model data at the acquisition time for descending tracks (17:00 UTM). Red and green circles highlight the ratio values for the dates of acquisitions. The best fitting sinusoidal function obtained using the daily NARR estimation is indicated by a red line. Triangles indicate the average delay/elevation ratio (in rad/km) estimated using pressure and temperature profiles provided by NARR and the water content profile provided by MERIS data, where available. Below, mean LOS velocity from data acquired by the Envisat satellite in a descending orbit between 2003 and 2006 (positive values indicate displacement towards the satellite). Results are superimposed on the SRTM Digital Elevation Model. The black box encloses the area of reference where the mean velocity is arbitrarily set to zero. NCV: Nevado de Colima Volcano, CV: Colima Volcano, GC: Guzman City, CC: Colima City, TF: Tamazula fault. After correction of individual wrapped interferograms using elevation-to-phase relationships estimated from the NARR model, phase-unwrapping was possible. The results show no significant widespread deformation, with only local subsidence of up to 30 mm/yr at the volcano summit and in Guzman City.

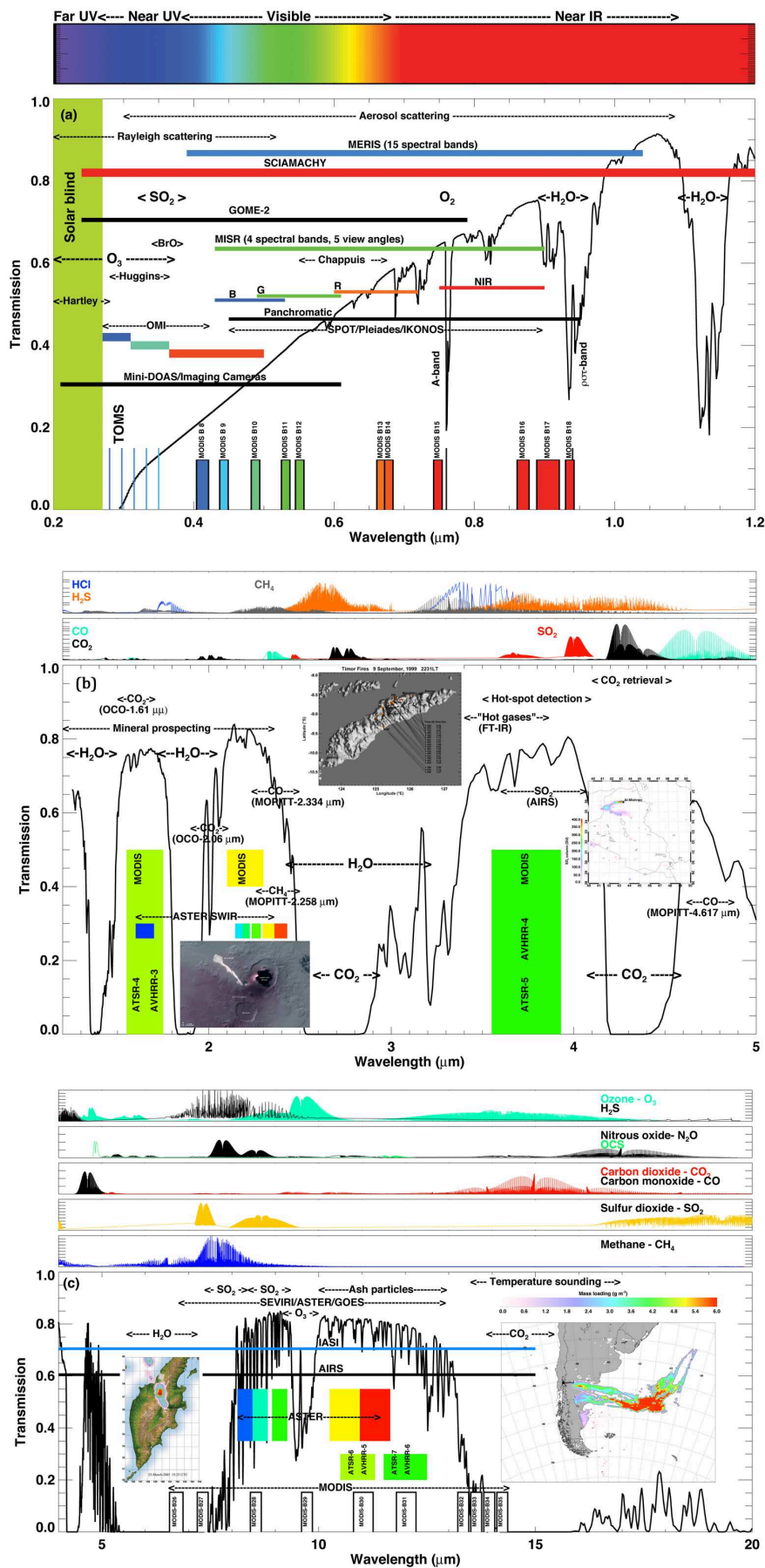


Fig. 10. (a) Vertical atmospheric transmission as a function of wavelength for the visible to near infrared part of the electromagnetic (EM) spectrum (black line). Also indicated are the regions where various atmospheric processes dominate

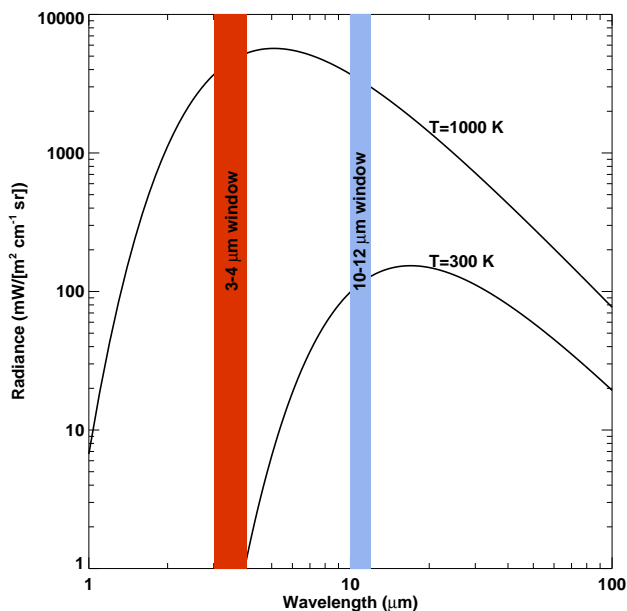


Fig. 11. Radiance as a function of wavelength for Earth temperatures at 300 K and 1000 K, typical of a warm surface heated by the Sun and a lava flow heated by the Earth's internal energy. The radiance for the hot lava at 1000 K peaks at lower wavelengths than that for the surface at 300 K.

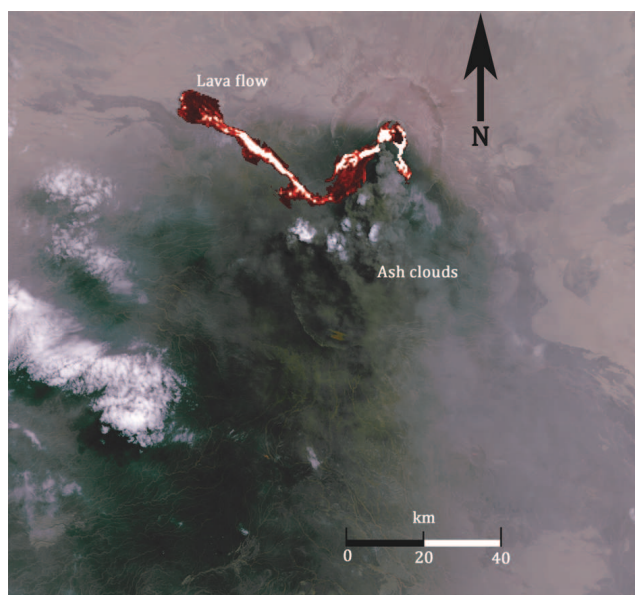


Fig. 12. ASTER image of Nabro volcano (Eritrea), in eruption. As well as the dark column of ash rising from the vent, a stream of hot lava (colored red-white) is evident. The eruption cloud was composed mostly of SO_2 – thought to be the largest single volcanic SO_2 emission since the eruption of Hudson, Chile in August 1991. Complete information for the ASTER image may be found at <http://photojournal.jpl.nasa.gov/catalog/PIA14390>. Image and processing courtesy of NASA/GSFC/METI/ERSDAC/JAROS, and U.S./Japan ASTER Science Team

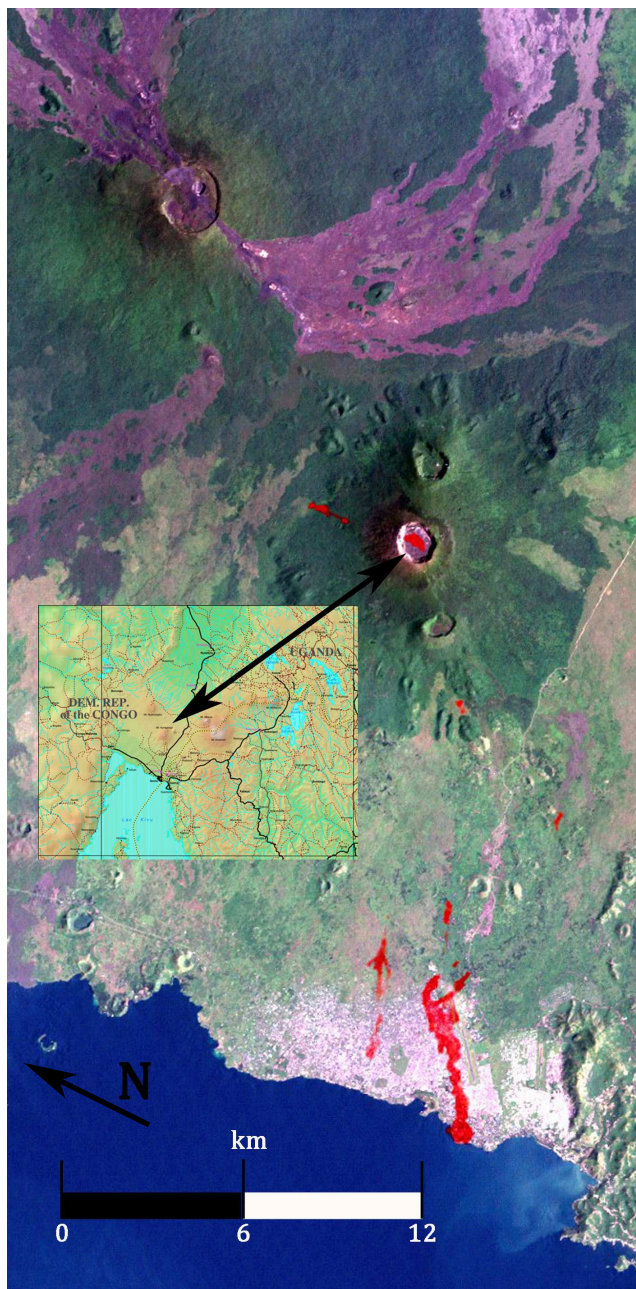


Fig. 13. ASTER, Landsat-7 and SRTM fused image of Nyiragongo volcano, DRC. Recent lava flows are colored red. The large crater to the north of Nyiragongo is Nyamuragira volcano, a prodigious source of SO_2 emissions. Lava has been identified (in red) through the city of Goma on the shore of lake Kivu, near the bottom of the image. A full description of the image and its processing may be found at <http://photojournal.jpl.nasa.gov/catalog/PIA03339>. mage and processing courtesy of NASA.

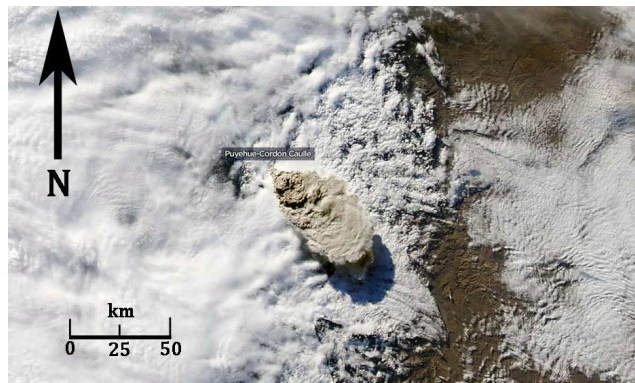


Fig. 14. MODIS true-color image of the initial plume rising from the Puyehue-Córdon Caulle eruption on June 5, 2011.

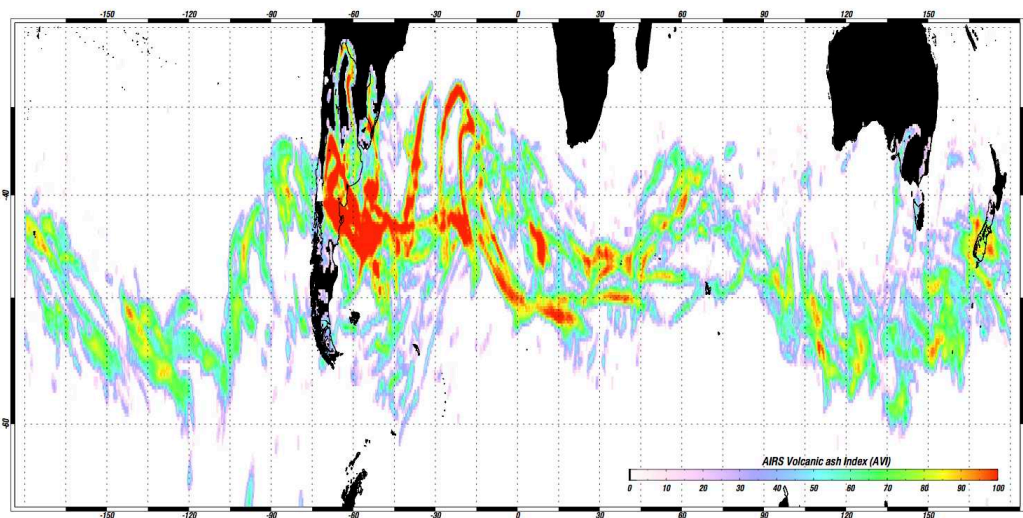


Fig. 15. Atmospheric InfraRed Sounder (AIRS) volcanic ash index (AVI) derived from brightness temperature spectra for the dispersing ash from Puyehue-Córdon Caulle eruption from June 5–25, 2011. AIRS could track the ash circumnavigating the southern hemisphere at least three times before the signal dropped below the detection limit. The location of Puyehue-Córdon Caulle is indicated by a white triangle.

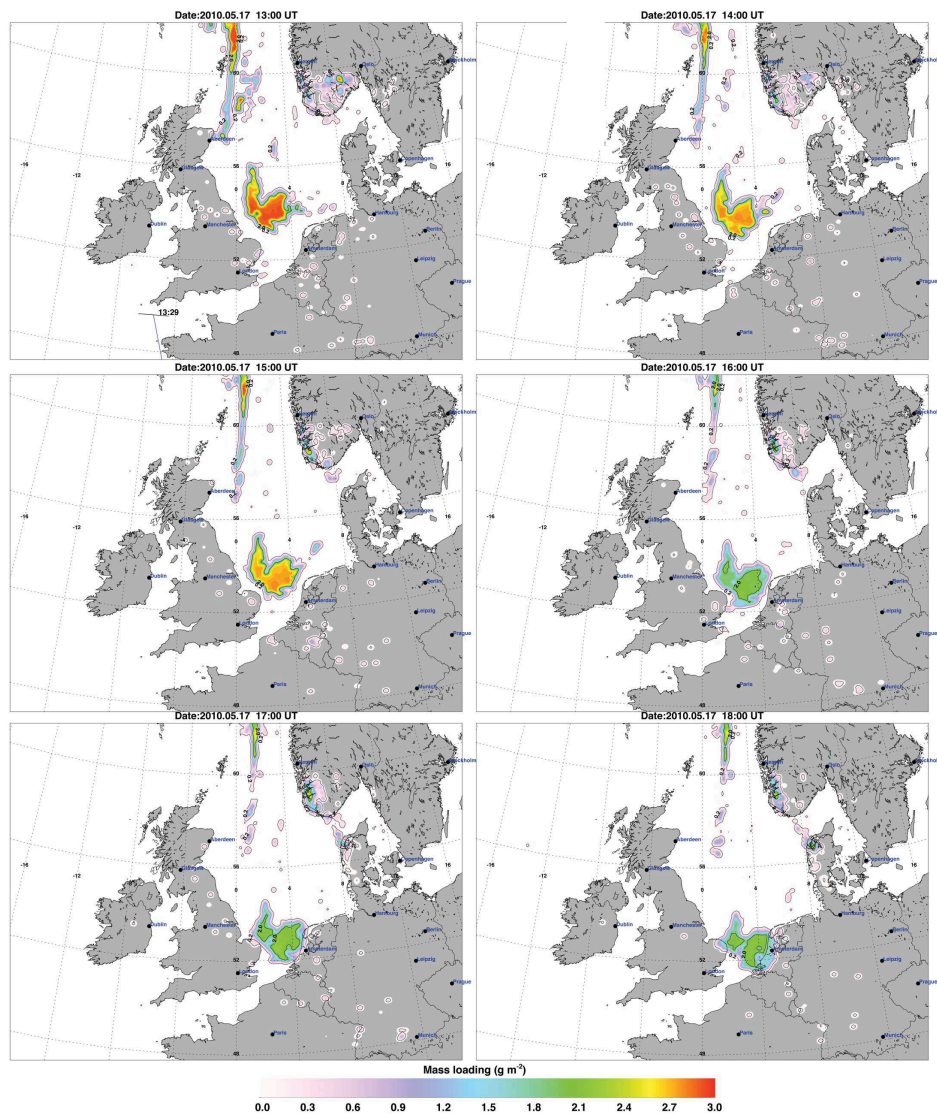


Fig. 16. Ash mass loading retrievals (in g m^{-2}) from the Meteosat-2 SEVIRI infrared measurements. Each panel is separated in time by one hour. The southward progression of a cloud of ash erupted from Eyjafjallajökull on 16 May, 2010 is clearly evident, as is the diminution of the mass loading as the cloud reaches the coast of Belgium and The Netherlands.

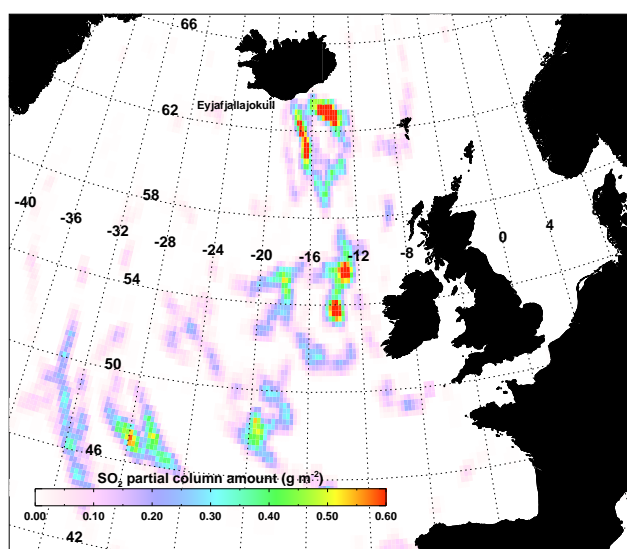


Fig. 17. SO₂ partial column amounts (g m⁻²) retrieved from the hyperspectral infrared AIRS instrument. The SO₂ emissions are from the Eyjafjallajökull eruptions between 5–13 May, 2010.